Received: Added at production | Revised: Added at production | Accepted: Added at production

DOI: xxx/xxxx

RESEARCH ARTICLE

Comparative Aerodynamic Analysis and Parallel Performance of 2D CFD Simulations of a VAWT Using Sliding Mesh Interface Method

Hüseyin Can Önel[1] | **Ali Ata Adam**[2] | **Nilay Sezer Uzol**[3]

[1]Department of Aerospace Engineering, Adana Science and Technology University, Adana, Türkiye

[2]Department of Engineering Science, University of Oxford, Oxford, UK

[3]Department of Aerospace Engineering, Middle East Technical University, Ankara, Türkiye

Correspondence

Corresponding Author Nilay Sezer Uzol, Middle East Technical University, Department of Aerospace Engineering, 06800 Çankaya, Ankara.

Email: nuzol@metu.edu.tr

Abstract

With rapid advancements in computer hardware and numerical modeling methods, Computational Fluid Dynamics (CFD) has gained prominence in simulating complex flows. As parallel computation becomes an industry standard, the computational efficiency of simulations has become critical. The flow around a Vertical Axis Wind Turbine (VAWT), characterized by complex dynamics and challenging rotating geometry, serves as an intriguing case for CFD studies. This study employs the open-source CFD solvers SU2 and OpenFOAM to simulate the incompressible, unsteady, and turbulent flow around an H-type Darrieus VAWT in two dimensions. Spatial and temporal discretization parameters are examined to balance computational cost and accuracy, revealing notable effects on power predictions. Simulations conducted under identical conditions allow for a comparison of the predictions and parallel performances of SU2 and OpenFOAM across three distinct tip speed ratios (TSRs). The findings show that discretization parameters behave differently at various TSRs. While power predictions from SU2 and OpenFOAM generally align with experimental data and with each other, discrepancies arise at lower TSRs, with thrust predictions showing better consistency. Although OpenFOAM provides a faster solution across all parallel configurations, SU2 demonstrates superior parallel scalability, achieving higher speedup and efficiency.

KEYWORDS

Computational Fluid Dynamics (CFD), dynamic mesh, Vertical Axis Wind Turbine (VAWT), parallel performance, SU2, OpenFOAM

1 | INTRODUCTION

Renewable energy sources have emerged as a crucial solution for reducing carbon emissions and meeting the escalating global energy demand. Among these sources, wind energy stands as a promising and rapidly growing sector, with wind turbines serving as the center of this development. Enhancing the design and efficiency of wind turbine rotors requires a profound understanding of complex aerodynamics, often accomplished through Computational Fluid Dynamics (CFD) simulations.[1,2] However, such complex unsteady fluid dynamics problems require high-fidelity solvers and powerful computational resources, leading to the development of computationally efficient frameworks to be used in High-Performance Computing (HPC) clusters for wind turbine applications.[3,4] Although pushing the understanding of flow around wind turbines forward, these types of solvers are usually developed in-house and close to public use. Open-source CFD flow solvers have gained significant interest in this field due to their versatility, accessibility, and receiving contributions from many researchers in the academic and industrial communities. However, computationally inefficient algorithms implemented in the solvers may cause significant CPU overhead, e.g., the sliding mesh algorithm widely used in the unsteady rotor simulations.[5] Moreover, the usage of open source flow solvers for a VAWT is highly limited in the literature as the vast majority of the studies[6,7,8,9,10,11,12,13,14] has preferred commercial solvers so far.

Vertical-axis wind turbines have been receiving a lot of attention from the wind energy community due to their simplicity and efficient usage on a small scale. H-type Darrieus wind turbines feature vertical rotor blades arranged in an ”H” shape around a central vertical shaft. They generate electricity as the wind flows past the blades, creating lift and causing them to rotate. Although they offer a reliable and omnidirectional operation, they may face challenges such as lower efficiency due to the significant interaction between the portions of the rotor facing upwind and downwind.[6] Therefore, this type of VAWT numerical analysis has become the focus of many research studies.

Computational studies on H-type Darrieus vertical axis wind turbines have typically focused on unsteady interactions between the rotor blades due to the vortices shed from the upwind blade reaching the downwind blade.[7] In addition, the angle of attack on the blades constantly varies over a large interval with azimuthal angle, which could lead to a dynamic stall. Due to the complex flow physics, the low-order models, such as the Blade Element Momentum (BEM) theory-based models, may not accurately predict the flow around the turbine blades.[15] On the other hand, Balduzzi *et al.*[6] showed that the CFD simulations of VAWTs could replicate the experimental results reasonably accurately, provided that the simulations run with a small time step and the mesh should be fine enough to accurately model the stall of the blades and resolve the vortices in the wake of the rotor. These spatial and temporal resolution requirements increase the computational cost of the simulations and force the researchers to employ HPC resources for the VAWT simulations.

The 3D VAWT CFD simulations may bring considerable insights into the effect of tip losses on the turbine performance.[8] Yet, they are not cost-effective and practically feasible for industrial applications due to highly increased computational cost compared to the accuracy gain.[9,4] At the same time, 2D simulations have demonstrated their ability to offer highly accurate predictions of both the overall performance and the flow characteristics around the rotor at a reasonable computational expense.[9]

The VAWT simulations require a fine spatial resolution due to the complex flow physics they involve. However, there is no approved mesh guideline on VAWT simulations.[6,16] In their review paper, Li *et al.*[16] explain that the adopted mesh convergence parameters, in this case, the General Richardson Extrapolation method and Grid Convergence Index (GCI), fail to present an accurate mesh-independent solution because the mesh convergence is not monotonous and the power value of the wind turbine fluctuates as also shown by[10,11]. Therefore, researchers have been focusing on conducting local mesh convergence studies rather than global mesh refinement to reduce the numerical inaccuracy of thrust and torque arising from the mesh resolution while minimizing the required computational cost of the simulations. The review of the computational VAWT studies in the literature is provided in Table 1 with the range of temporal and spatial resolution parameters they adopted. In addition, the diameter of the rotating zone (Interface) and the distance of the domain boundaries (Inlet, Outlet, and Lateral) from the rotor center are given as normalized by the rotor diameter D.

Many studies showed that an accurate prediction of the boundary layer on the rotor can be achieved with a mesh resolution giving $y^+ < 2$.[17,6] In addition, the number of cells around the rotor blades and within the rotor region has been the focus of many studies. The number of surface nodes and boundary layer resolution are the focal point of the mesh refinement in[6] where at least 500 nodes on the airfoils with a boundary layer resolution in the order of $y^+ \sim 1$ are shown to be required for a mesh resolution convergence. Similarly, Nguyen *et al.*[4] refined the mesh resolution around the rotor for their VAWT simulations. In addition, they conducted an automated adaptive mesh refinement to reduce the error indicator of the cells, which is based on the solution of an adjoint problem to the Navier-Stokes equations. The refinement resulted in reduced cell sizes around the rotor and wake region. However, the end result is a mesh with more than a million vertices, which could be deemed practically infeasible from a computational point of view. Also, the discretization on the rotating zone interference, i.e., the resolution in the circumferential direction, is shown

List of Abbreviations and Symbols: SMI: Sliding Mesh Interface, C_P: Power coefficient, c_p: Pressure coefficient, D_{SMI}: Diameter of the SMI, D: Rotor diameter, $\Delta\Theta_t$: Azimuthal increment per time step, Θ_R: Azimuthal position of the rotor, Θ_i: Azimuthal position of a blade i with respect to its initial position, Δx: Cell edge length, N_{AF}: Number of grid nodes on a blade section, N_{SMI}: Number of grid nodes on the SMI, λ: Tip Speed Ratio (TSR), N_{OI}: Number of outer iterations.

to affect the development of vortices in the turbine wake.[18] In addition, the lateral and longitudinal extent of the domain could affect the flow field and turbine performance parameters due to the blockage effect of the lateral boundaries and the wake development downstream of the rotor.[6,9]

Due to the complex unsteady blade-wake interactions in the turbine, the temporal resolution of the VAWT simulations is an important variable as much as the mesh refinement. A sufficiently low time step could better resolve the vortices in the flow and stabilize the simulation, thus predicting a consistent power production. In addition, taking a lower time step could lessen the requirement of a mesh refinement.[7] This shows that the required spatial resolution could be coupled with the temporal resolution. This coupling can be represented by the non-dimensional Courant number, $Co = V\Delta t/\Delta x$, where V is the flow speed in a cell and Δx is the cell size. Balduzzi *et al.*[7] showed that the average Co around the domain should be kept $Co < 5$. Nevertheless, Co may not be the sole temporal resolution regulator, as a universal temporal resolution requirement for VAWT simulations has yet to be agreed upon. This mainly results from the effect of λ on the flow characteristics. λ is the tip speed ratio, defined as the linear speed at the tip of the rotor due to rotation divided by the freestream velocity. As a low λ causes significant vortex shedding from the blades, a lower time step is required for lower tip speed ratios.[7,9,12] Therefore, the time step values used in the literature ranges from 0.02° to 2°, as shown in Table 1.

TABLE 1 Review of the 2D computational studies on VAWTs.

Work	Spatial resolution			Distance to the rotor (D)				Temporal resolution	
	Mesh size	y^+	# Surface nodes	Interface	Inlet	Outlet	Lateral	Δt (°)	N_{OI}
Balduzzi *et al.*[6]	350k	1	523	2	40	100	30	0.27 - 0.405	30
Balduzzi *et al.*[7]	350k - 1.5M	1	523 - 1794	2	40	100	30	0.135 - 0.405	
Maalouly *et al.*[8]	347k	1	Not given	1.41	10	15	7.5	0.25	
Bianchini *et al.*[9]	860k	1	900	1.5	12	24	18	0.14, 0.23	
Meana-Fernández *et al.*[10]	990k	1	520	5.5	6	6	N/A	0.25	
Almohammadi *et al.*[11]	53k - 2.17M	1	300 - 7552	2.8	3.5	10.5	4	0.02 - 0.2	
Balduzzi *et al.*[12]	182k - 817k	1	782 - 2698	2	40	100	30	0.068 - 0.54	
Abdalrahman *et al.*[13]	Not given			2.941	40	100	30	Not given	
Rossetti & Pavesi[14]	464k	5	Not given	1.4	4	8	2.65	2	
Maître *et al.*[17]	100k	1.6	Not given	1.7	2	3.7	2	2	75
McNaughton *et al.*[18]	280k	1	170	1.1	5.5	5.5	2	0.002	

In this study, the aerodynamic performance of a VAWT rotor is simulated with open-source CFD solvers OpenFOAM and SU2 on an HPC system. This study aims to investigate how the computational parameters and methods used for the rotor simulations affect the ability of the CFD solvers to make accurate aerodynamic performance predictions for VAWT rotors. In addition, the computational cost and parallel computing performance of the solvers for this VAWT test case are discussed.

2 | METHODOLOGY

2D Unsteady Reynolds-Averaged Navier-Stokes (URANS) parallel CFD simulations of a VAWT test case are performed by using the open-source flow solvers OpenFOAM and SU2 by using structured grids with the Sliding Mesh Interface (SMI) methodology as described below. Both flow solvers are compiled with GNU CC and OpenMPI and run in parallel on the available HPC systems for this study.

2.1 | VAWT Test Case

In this work, a widely studied[6,7,13,19] 3-bladed H-type Darrieus wind turbine is selected as a VAWT test case. The main features of the 3-bladed rotor with rectangular planform blades are given in Table 2.

2.2 | Flow Solvers and Simulation Parameters

The unsteady flow around the 2D VAWT is simulated numerically by solving the URANS equations, which include the conservation of mass, momentum, and turbulence quantities (the turbulent kinetic energy k and its specific rate of dissipation ω). The parallel computations are performed using the open-source flow solvers OpenFOAM[20] and SU2[21] based on Finite Volume (FV) method.

TABLE 2 VAWT test case geometry information

VAWT Geometry Summary	
Number of Blades	3
Blade Airfoil	NACA 0018
Rotor Radius (m)	0.85
Airfoil Chord (m)	0.246
Rotation Direction	Counter-Clockwise (CCW)

The governing equations for the simulations are the conservation of mass and momentum equations for an incompressible, unsteady, and turbulent flow, which are given in Eq. 1 and Eq. 2, respectively.

$$\frac{\partial(u_i)}{\partial x_i} = 0 \tag{1}$$

$$\frac{\partial(u_i)}{\partial t} + u_j \frac{\partial(u_i)}{\partial x_j} = -\frac{1}{\rho}\frac{\partial(p)}{\partial x_i} + \frac{\partial}{\partial x_j}\left[2\nu S_{ji} - \frac{1}{\rho}\overline{u_j' u_i'}\right] \tag{2}$$

Here; the strain rate tensor is $S_{ij} = \frac{1}{2}\left(\frac{\partial(u_i)}{\partial x_j} + \frac{\partial(u_j)}{\partial x_i}\right)$, and the Reynolds stress tensor is $-\overline{u_j' u_i'} = 2\nu_t S_{ij} - \frac{2}{3}k\delta_{ij}$ based on the Boussinesq approximation. It should be noted that the linear speed of the blade tips does not exceed $U_{\text{tip}} = 25m/s$, which corresponds to $M_{\text{tip}} = 0.073$. Thus, the flow can be assumed incompressible.

Turbulence is modeled with the low-Reynolds $k-\omega$ SST model proposed by Menter *et al.*[22] with its default model parameters. This turbulence model was suggested for the simulations of Darrieus wind turbines due to its accurate modeling of flow separation and free-shear flow among the eddy-viscosity-based models.[6,23] In this model, the turbulence quantities, turbulent kinetic energy (k), and its specific rate of dissipation (ω) are governed by equations Eq. 3 and Eq. 4, respectively.

$$\frac{\partial(k)}{\partial t} + u_j \frac{\partial(k)}{\partial x_j} = \frac{\partial}{\partial x_j}\left(D_k \frac{\partial(k)}{\partial x_j}\right) + G - \beta^* \omega k + \frac{S_k}{\rho} \tag{3}$$

$$\frac{\partial(\omega)}{\partial t} + u_j \frac{\partial(\omega)}{\partial x_j} = \frac{\partial}{\partial x_j}\left(D_\omega \frac{\partial(\omega)}{\partial x_j}\right) + \frac{\gamma G}{\nu} - \beta\omega^2 - \left(F_1 - 1\right) CD_{k\omega} + \frac{S_\omega}{\rho} \tag{4}$$

A complete explanation of each term in these equations is omitted here for conciseness, and the reader is referred to the papers by Menter[24] and Menter *et al.*[22]. For all the conducted simulations, the model parameters are set to their default values.

The computational domain is 2D and discretized into cells, as shown from different views in Fig. 1. For the SU2 simulations, the hybrid unstructured mesh consists of triangular and quadrilateral cells, whereas OpenFOAM requires a 3D grid of cells with a finite spanwise thickness. Therefore, the same mesh used in SU2 simulations is extruded in the third dimension for OpenFOAM. However, there is only one layer of planar prism and hexahedron cells in the spanwise direction to prevent any 3D effects. More details on the computational mesh are given in Sec. 3.1.

The shape and dimensions of the computational domain are shown in Fig. 2. The inlet, outlet, and side boundaries are placed far away from the rotating region to prevent any blocking effects, and their values are selected from the comparisons in Table 1.

At the inlet of the domain, Dirichlet-type boundary conditions are given for u_i, k, and ω, and zero gradient pressure is defined. k and ω are adjusted for 5% turbulence intensity and $\mu_t/\mu = 10$ eddy viscosity ratio. Zero gauge pressure is imposed at the outlet, while other variables are set to zero gradient. Symmetry boundary conditions are used at the lateral boundaries of the domain. At the blade walls, the no-slip condition (i.e., zero relative velocity), and the pressure has zero gradient normal to the surface. k is set to zero, and automatic wall treatment is used for ω.

2.2.1 | OpenFOAM

OpenFOAM[20] is an open-source CFD toolbox written in C++. In this study, its incompressible flow solver (*pisoFOAM*) and dynamic mesh libraries are primarily used.

Second-order accurate Crank-Nicolson time integration is performed. Likewise, the same order of accuracy is obtained in space with Gaussian integration for gradient, divergence, and interpolation operations using linear upwinding for momentum. First-order upwinding is utilized for turbulence quantities. The well-known pressure-velocity decoupling in the solution of pure incompressible flows is handled by a combination of Pressure Implicit with Split Operator (PISO)[25] and Semi-Implicit Method for Pressure-Linked Equations (SIMPLE)[26] algorithms, which solves the equations sequentially. This combination allows large time steps beyond the CFL (Courant–Friedrichs–Lewy) condition[27], i.e., $\Delta t < (\Delta x/U)_{\max}$

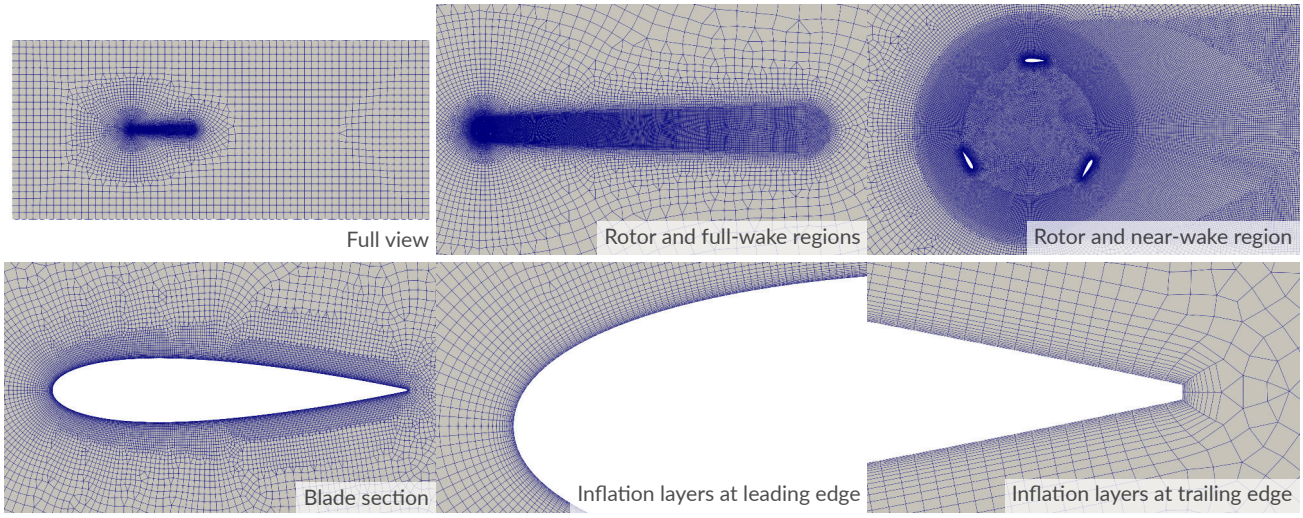

FIGURE 1 2D computational mesh used in the CFD simulations of VAWT

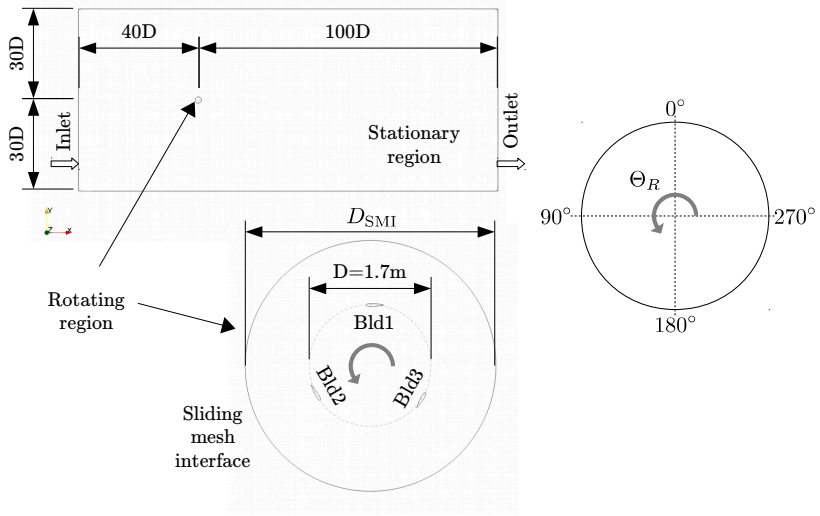

FIGURE 2 Dimensions of the computational domain (top) and the rotor region (bottom), and definition of the rotor azimuthal positions (Θ_R)

can be exceeded, where Δx and U are the local cell size and flow speed, respectively. The residuals are ensured to drop to 10^{-5} for numerical convergence.

The domain is decomposed using the SCOTCH algorithm[28], which employs a non-hierarchical method that balances the computational load by distributing the cells among the processors as evenly as possible and minimizing the communication interfaces. An example grid decomposed into 8 subdomains can be seen in Fig. 3. A processor may adopt cells from different regions in the case of a sliding mesh simulation, as in the case of processor 4. Also, the cell-processor assignment remains constant as the dynamic region rotates (Fig. 3).

The PISO algorithm is subject to the CFL (Courant–Friedrichs–Lewy) condition,[27] which relates the grid size to advection speed. To ensure numerical stability, an adaptive time-stepping algorithm is utilized to keep the time step size $\Delta t < (\Delta x/U)_{max}$, where Δx and U are the local cell size and flow speed, respectively.

2.2.2 | SU2

SU2 is an open-source flow solver written in C++ programming language. It comprises several components, including a PDE solver, *SU2_CFD*. It can solve RANS equations in parallel with Message Passing Interface (MPI) and using the mesh graph partitioning library ParMETIS. An edge-based

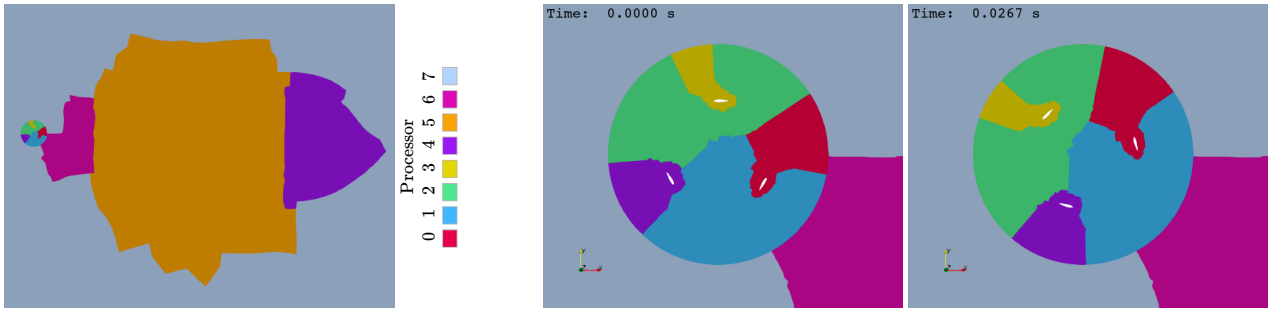

(a) Processor assignments

(b) Rotating region at $\Theta_R = 0^\circ$ (left) and 45° (right) azimuthal positions

FIGURE 3 The solution domain decomposed into 8 processes in OpenFOAM

data structure is adopted in SU2 with the finite volume method. Flux terms are evaluated at the midpoints of the edges and discretized using the second-order flux difference splitting (FDS) scheme with the Monotonic Upstream-centered Scheme for Conservation Laws (MUSCL) approach.

The incompressible RANS equations are solved with a density-based solution approach and Chorin's artificial compressibility method[29] in SU2. In this approach, the density is initially assumed to be a function of pressure and temperature as $\rho = \rho(P, T)$, although it is constant for an incompressible fluid. Therefore, the partial derivative of density with respect to pressure appears in the governing equation. This derivative is replaced by a factor based on the maximum speed squared in the solution domain and updated at each simulation time step. This factor affects the convergence of the simulation rather than its results.[30] For more details on this computational approach, refer to[30].

SU2 performs two nested loops for a time-dependent simulation for an increased convergence rate. The time step is marched by a second-order dual time-stepping approach, using the backward finite difference method. In the iteration loop within a physical time step, a pseudo-time marching is performed by an Euler implicit method. The linear system in the pseudo time step is solved using the flexible generalized minimal residual (FGMRES) method[31], which iteratively approximates the solution of the linear system in the form of a Krylov subspace vector with minimum residual. The Incomplete Lower Upper (ILU) factorization, which is a sparse approximation of the LU factorization of the system, is combined with the FGMRES method as a preconditioner for faster convergence. The linear solver runs until the linear solver residual reaches 10^{-10} for a maximum of 10 iterations, as suggested in[30].

2.3 | Dynamic Mesh

For the unsteady VAWT simulations, dynamic mesh capability is used in both flow solvers.

2.3.1 | OpenFOAM

OpenFOAM's built-in capabilities are utilized for the simulations with a Sliding Mesh Interface (SMI), enabling communication across disconnected and adjacent mesh domains. A special boundary condition couples separate meshes at non-matching periodic domain boundaries. This boundary condition is also capable of operating in a parallelized environment. Among the various alternatives, the SMI method stands out for its efficient handling of dynamic mesh deformations. This method demonstrates superior computational cost compared to the Overset Mesh method[32] and higher accuracy than the Multi-Reference Frame method[33].

To calculate the face fluxes across the SMI, a face area weighted interpolation method is utilized. Figure 4 shows the sample cells neighboring the sliding interface. Here, each color indicates which processor a cell belongs to. If cell N6 is considered, its f_2 and f_3 faces remain within the rotating domain, while f_1 face lies on the SMI. On f_1, the flux contribution across the SMI comes from the cells N1 and N3. In that case, the total flux through f_1: $\phi_{N1} + \phi_{N3}$ is weighted according to lengths of $|ab|$ and $|bc|$. This example involves parallel communication between 3 processors: p0, p1 and p2. Since the rotating domain moves, a simulation with SMI requires recalculation of the moving cells, face neighbors, and their parent processors at each time step. Also, the mesh data is written to the disk at the I/O steps. Hence, the overhead of these operations should be considered in the simulation.

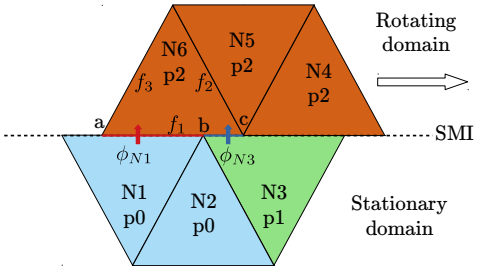

FIGURE 4 Inter-processor communication across the SMI during a parallel OpenFOAM run

2.3.2 | SU2

In the multi-zone problems involving a SMI, SU2 creates a halo layer around each mesh partition for communication between the zones. Initially, the halo layer is defined by the nearest neighbor search for nodes and elements adjacent to the sliding interface, called the donor zone. Then, the layer is used to generate a new mesh with updated connectivity and a communication schedule for nearest-neighbor communications. The communications of the data are done using non-blocking MPI functions `MPI_Isend` and `MPI_Irecv` and the usage of `MPI_Waitany` ensures that all non-blocking send and receive calls are completed. Once the new mesh is set up, the relative motion of the zones is applied, which results in non-coincident halo layers. Therefore, a search and interpolation routine is used to identify the coinciding cells in the donor zone and halo layer and interpolate the data to the halo node. In this work, the interpolation routine is performed using a conservative weighted average approach. This sliding mesh method has been acknowledged to be computationally inefficient for massively parallel simulations .[34] Even though the solver was updated with a more computationally efficient implementation[35], a demonstration of the scalability of this approach has not been presented in the literature to the best of the authors' knowledge.

3 | RESULTS AND DISCUSSIONS

In this section, the flow solutions obtained from SU2 and OpenFOAM are presented. First, a discretization convergence study is conducted to determine the optimal spatial and temporal resolutions at various tip speed ratios. The simulation's sensitivity to the size of the rotating region is tested with multiple SMI diameters, and the wake refinement level is assessed. After identifying the best-performing parameters, these are used to obtain full-length solutions with both SU2 and OpenFOAM. The flow fields predicted by both solvers in the rotor and wake regions are investigated and compared, along with their power and thrust predictions. Finally, the parallel performances of SU2 and OpenFOAM are assessed.

In the following simulations, the flow domains are initialized with uniform field variables. Consequently, approximately 20 revolutions of simulation time are allowed before calculating the averages, which provides a sufficiently developed flow field.[36] After reaching statistical steadiness, samples are taken from an additional three revolutions.

To see the effect of the rotational speed, three distinct tip speed ratios are considered in the simulations: i) low TSR (λ = 1.31), ii) rated (medium) TSR (λ = 2.36), and iii) high TSR (λ = 3.14). The exact values are decided based on the experimental results of Balduzzi *et al.*[6].

3.1 | Analysis of Computational Sensitivity to Spatial and Temporal Discretization

The tradeoff between accuracy and computational cost is critical in numerical flow simulations. To ensure that the spatial and temporal discretizations are sufficiently fine, yet computationally economical, a convergence study is conducted first. As proposed in the previous similar studies, the main discretization parameters are:

- node spacing in the rotating region, which is determined by the airfoil node count (N_{AF}) and the SMI node count (N_{SMI}),
- time step size (Δt), which is often characterized by the azimuthal increment per time step ($\Delta\Theta_t$) in dynamic mesh simulations with rotating geometries.

In addition to these, a systematic survey on the SMI diameter (D_{SMI}), the wake region refinement level (Δx_W), and the number of outer iterations (N_{OI}) within a time step are also conducted in this study, which was not given much attention in the previous studies. The refinement level of the boundary layer in the wall-normal direction is unchanged in this analysis as the requirement for this parameter has already been set in the literature,

and the established guidelines have been adopted in this work. The power coefficient of the rotor C_P is chosen as the convergence criterion since both numerical and experimental reference values are available in the literature.[6] The analyses in this section are conducted with SU2. For a VAWT, the power coefficient is calculated as $C_P = P/P_{wind}$. Here, the rotor power is $P = M_z\Omega$ (M_z: torque around the z-axis, Ω is the rotor speed in rad/s), and the available power in the wind for the rotor swept area is $P_{wind} = 0.5\rho U_\infty^3 D$. Unit depth ($z = 1\ m$) is considered in area and span calculations.

3.1.1 | Grid Convergence Study

As the VAWT rotates, each blade dynamically moves through the wake of the upstream blades. Thus, it is necessary to generate a uniformly spaced mesh in the rotating region, and its refinement level becomes vital in capturing the advection of the wake of the upstream blades, where high-gradient field variables are present. A significant portion ($\approx$ 55%) of the total cells lie within the rotating region. To determine the node spacing, six grids of various sizes are tested. Mesh details are given in Table 3. The grid size is controlled by changing the number of nodes on both the airfoils (N_{AF}) and the SMI (N_{SMI}). Other simulation parameters are kept constant: the azimuthal increment per time step $\Delta\Theta_t = 0.5°$, and the SMI diameter $D_{SMI} = 1.5D$. In Table 3, $\Delta\Theta_{SMI}$ shows the arc angle between the nodes on the SMI, which relates how much the interface travels per time step. Regardless of the value, the face fluxes are successfully calculated with the area-weighted approach. From the coarsest grid (F) to the finest (A), the number of nodes on the airfoils and SMI, as well as the cell size within the rotating region, changes by a factor of 3.33. Between each subsequent refinement, the grid size increases by approximately 30%. The first cell height on the airfoil walls is set to 5×10^{-5}m, and 13 inflation layers are utilized with an expansion ratio of 1.2 in all meshes. This ensures the grid remains within the viscous sublayer and resolves the boundary layer accurately. The average y^+ is kept below 2, with a maximum around 5, ensuring a proper boundary layer resolution. The resulting grids are shown in Fig. 5.

TABLE 3 Details of the computational grids used in the grid convergence study

	A	B	C	D	E	F
N_{AF}	520	480	390	260	194	154
N_{SMI}	720	664	540	360	270	216
Δx_{SMI} (m)	0.01113	0.01205	0.01484	0.02225	0.02967	0.03709
$\Delta\Theta_{SMI}$ (°)	0.500	0.542	0.667	1.000	1.333	1.667
Number of cells	180,475	160,537	118,822	69,880	49,200	38,420

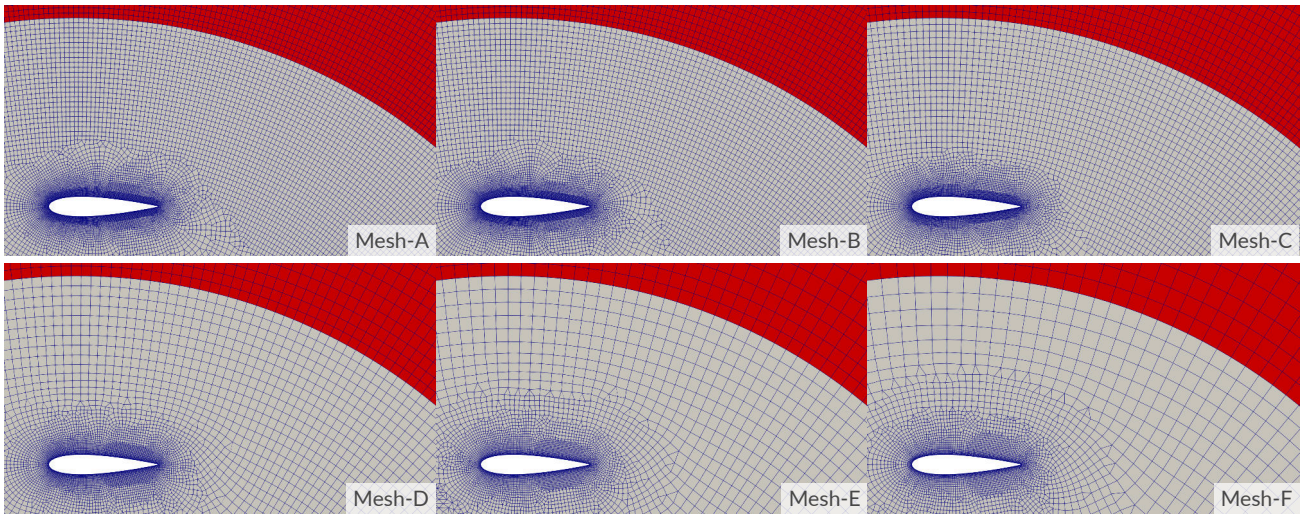

FIGURE 5 Meshes used in the grid convergence study (red color marks the non-rotating region)

The power coefficient (C_P) values predicted in the test cases are shown in Fig. 6. At lower tip speed ratios, the predicted power continuously increases as the mesh gets finer. The most extensive variation in C_P from the coarsest (F) to finest mesh (A) is observed as 45% at the lowest tip

speed ratio of $\lambda = 1.31$. The rate of change slows down after Mesh-C and C_P varies only 5% from Mesh-B to Mesh-A. The coarsest-to-finest C_P variation is somewhat milder as 14.5% at the rated TSR of $\lambda = 2.36$. The power prediction seems to be converged at Mesh-D, where an additional level of refinement to Mesh-C changes C_P by a marginal value of 0.3%. Likewise, further refinements provide slight improvement. Conversely, the variation is non-monotonous at the highest TSR of $\lambda = 3.14$, as was reported in previous studies.[12] From the coarsest Mesh-F to Mesh-B, C_P varies between 0.063 and 0.032, corresponding to a $\pm$16% range around the mean value. Only at the final refinement step, the predicted power reaches a terminal value.

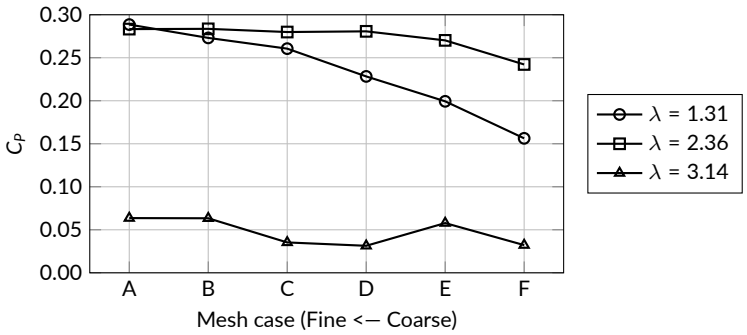

FIGURE 6 Variation of the power coefficient C_P with mesh resolution at three different λ: 1.31, 2.36 and 3.14. The mesh resolution becomes finer from mesh case F to A.

Each rotational speed yields a unique grid convergence trend. It should be noted that since other simulation parameters have yet to be tested, the goal here is to obtain a converging trend rather than reach the absolute power measurements. Thus, Mesh-B is chosen as the optimal computational grid and is used for the following simulations.

3.1.2 | Sensitivity to SMI diameter

The diameter of the rotating region constitutes the dynamic part of the mesh that rotates. Understanding how varying this diameter influences the solution, particularly in terms of power prediction, could be crucial. This section aims to identify the optimal size that balances computational efficiency and accuracy by testing four different diameters. Mesh-B is chosen as the base mesh with $D_{SMI} = 1.5D$, and one smaller ($D_{SMI} = 1.25D$) and two larger diameters ($D_{SMI} = 1.75D$ and $2.0D$) are tested (Fig. 7). A larger diameter may capture more wake effects and blade-flow interactions, leading to more precise simulations but at increased computational cost. Conversely, a smaller diameter might reduce computational demands but risks oversimplifying flow dynamics and causing interference with turbine blades and the sliding interface.

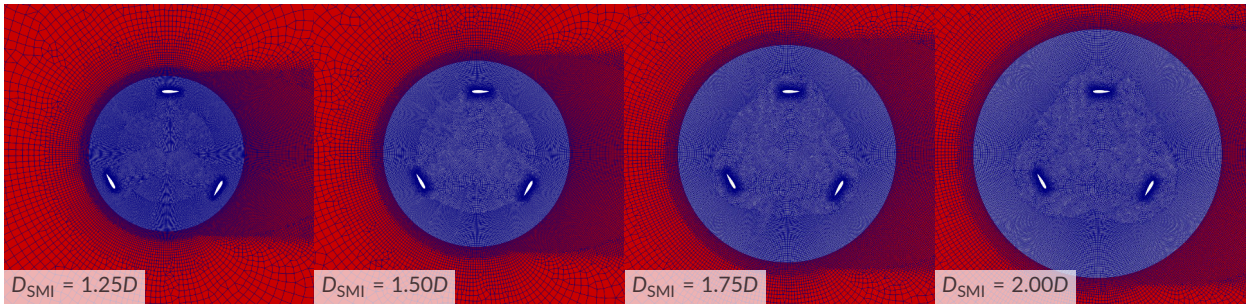

FIGURE 7 Meshes used in the SMI diameter sensitivity study (red color marks the non-rotating region)

Table 4 lists the mesh details. To keep the background cell size within the rotating region constant in all meshes, the number of nodes along the SMI is set such that the spacing is constant at $\Delta x_{SMI} = 1.21 \times 10^{-2}$ m. Accordingly, the azimuthal spacing (arc angle) between the nodes ($\Delta\Theta_{SMI}$) decreases as the diameter gets larger, which is important in terms of time step sizing. However, this variation is marginal, ranging only from 0.41° to 0.65°. At each step of D_{SMI} increase, the number of cells increases by approximately 10%.

TABLE 4 Details of the meshes used in the SMI diameter sensitivity study

	D_{SMI} = 1.25D	D_{SMI} = 1.50D	D_{SMI} = 1.75D	D_{SMI} = 2.00D
$\Delta\Theta_{SMI}$ (°)	0.650	0.542	0.464	0.405
N_{SMI}	554	664	776	888
Number of cells	145,295	160,537	178,818	197,706

Results in Fig. 8 show that changing the SMI diameter causes less than 1% variation in the predicted rotor power at all three TSRs. This small variation is attributed to slight variations in the mesh and its reflection on numerical convergence. In conclusion, even D_{SMI} = 1.25D provides enough distance from the blades to avoid interference, and the simulation is fairly insensitive to the rotating region diameter. This also indicates that the flux calculations across the SMI interface are handled accurately. Accordingly, D_{SMI} = 1.5D is chosen for the following simulations.

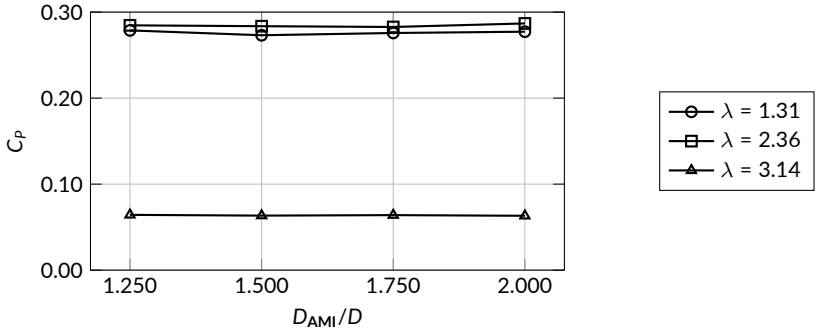

FIGURE 8 Variation of the power coefficient C_P with diameter of the rotating domain D_{SMI} at three different λ: 1.31, 2.36 and 3.14.

3.1.3 | Sensitivity to Wake Refinement

In cases with significant flow separation, recirculation, or flow reversal, the downstream flow can influence the upstream conditions. This is particularly important in turbulent flows, flows over bluff bodies, or flows with strong adverse pressure gradients. The pressure field in a fluid flow is governed by elliptic equations, meaning pressure changes can propagate upstream. This is especially evident in incompressible flows where pressure waves travel instantaneously throughout the domain. Thus, the impact of the grid resolution at the wake region on the rotor power prediction is investigated in this section.

The wake refinement effect is tested on three distinct meshes, as shown in Fig. 9. Mesh-B, as found in the previous section, is used as the base (medium) density mesh. To obtain a finer grid, the cell size is halved at the beginning (rotor) and the end of the wake refinement cone, which doubles the cell count from 160k to 322k (Table 5). A third grid is also generated, where the wake refinement is completely removed, reducing the cell count by 35% from 160k to 103k. The node spacing within the rotating region is identical in all three meshes.

TABLE 5 Details of the meshes used in the wake refinement sensitivity study

	Fine	**Medium**	**None**
Δx at rotor (m)	3.014×10^{-3}	1.205×10^{-2}	No refinement
Δx at far wake (m)	3.014×10^{-2}	1.205×10^{-1}	No refinement
Number of cells	322,269	160,537	103,095

Figure 10 shows the predicted power with different wake refinements. Both at λ = 1.31 and λ = 2.36, the difference in C_P between no wake and finest wake cases is less than 1%. At the highest TSR λ = 3.14, generating a medium refinement in the wake region changes the power prediction by a dramatic amount of 22%. However, a further refinement from medium to fine causes a mild power variation of 7%. This is attributed to the stronger pressure fluctuations in the near wake due to the higher rotation speed and turbulence generation. The medium-refined wake offers a better computational trade-off because the computational cost between the medium and fine meshes is approximately two-fold. Moreover, the

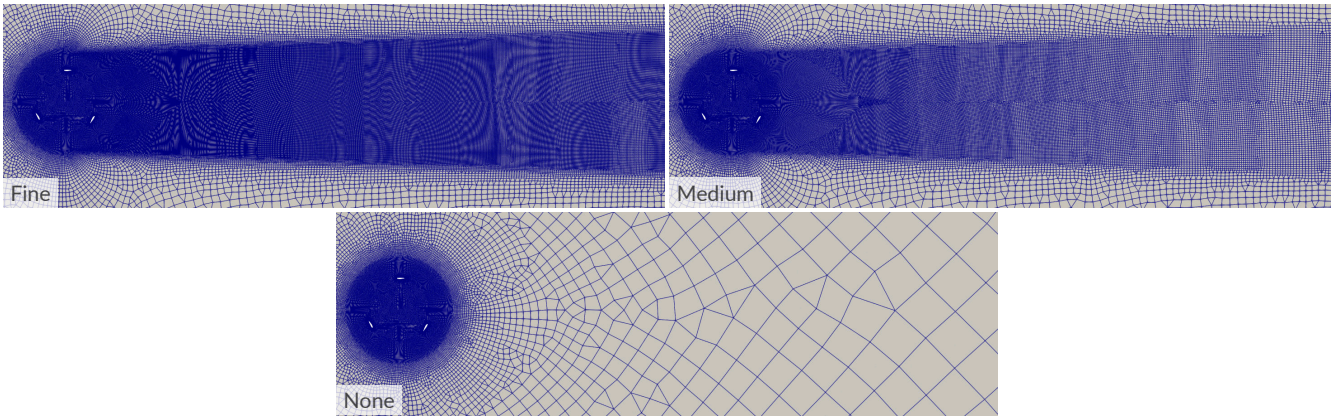

FIGURE 9 Meshes used in the wake refinement sensitivity study

wake structures are of interest in the following sections. As seen in Fig. 11, a wake refinement is crucial in capturing high-gradient wake dynamics. Thus, the medium wake refinement is used in the rest of the study.

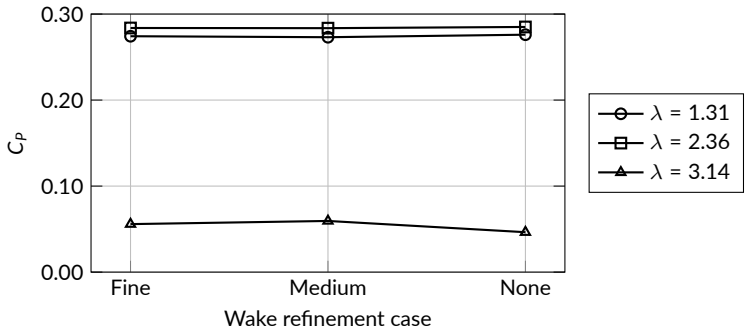

FIGURE 10 Variation of the power coefficient C_P with wake refinement level at three different λ: 1.31, 2.36 and 3.14.

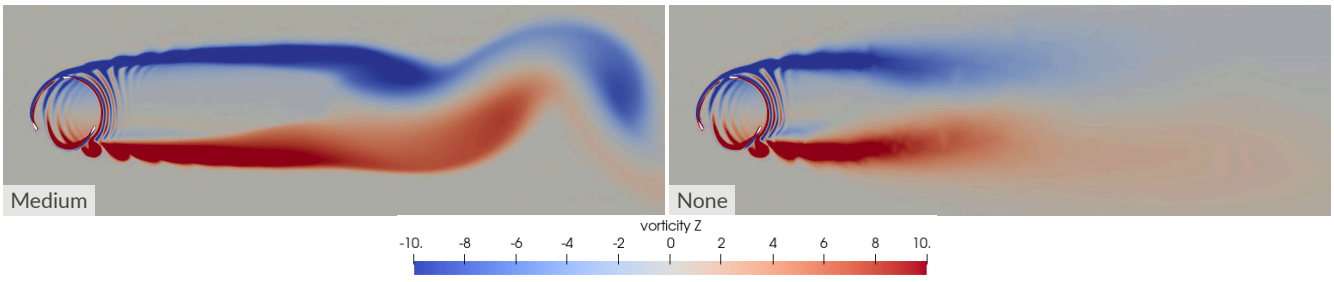

FIGURE 11 Vorticity (s^{-1}) contours in the far wake region with medium-level wake refinement (left) and without wake refinement (right) at λ = 2.36

3.1.4 | Temporal Convergence Study

In CFD simulations for VAWTs using a sliding mesh approach, the choice of azimuthal increment for time steps and the number of outer iterations per time step is crucial for accuracy and efficiency. These parameters affect the simulation's ability to capture the unsteady aerodynamic phenomena

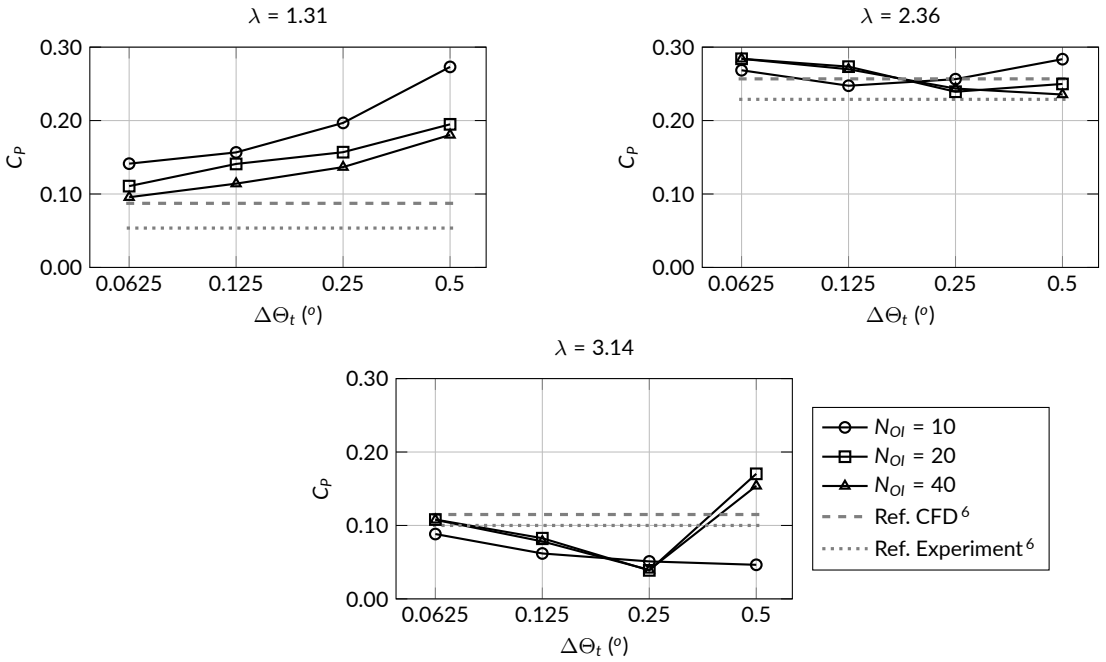

FIGURE 12 Variation of the power coefficient C_P with azimuthal time step increment ($\Delta\Theta_t$) at λ = 1.31 (top-left), λ = 2.36 (top-right), and λ = 3.14 (bottom) from the CFD predicitons with multiple N_{OI} and reference CFD and experiment values from [6]

of VAWTs under varying tip speed ratios (TSRs). The azimuthal increment determines the resolution of the rotor's movement, while the number of outer iterations ensures solution convergence within each rotor movement. Optimizing these parameters balances computational cost and simulation fidelity. At different TSRs, changes in aerodynamic loading and flow separation require adaptive simulation parameters. A finer azimuthal increment improves resolution but increases computational expense, while too few iterations can cause convergence issues and inaccuracies. This section provides guidelines for efficient simulations by examining these factors.

Figure 12 illustrates the power coefficient (C_P) as a function of the azimuthal increment ($\Delta\Theta_t$) for different numbers of outer iterations (N_{OI}) at three different tip speed ratios. At λ = 1.31, a clear trend is observed where the C_P decreases significantly with finer azimuthal increments. There is an almost two-fold variation in power from $\Delta\Theta_t$ = 0.5° to $\Delta\Theta_t$ = 0.0625°. A clear convergence can not be found when $\Delta\Theta_t$ = 0.5° is refined to $\Delta\Theta_t$ = 0.25° with none of the N_{OI} cases. From $\Delta\Theta_t$ = 0.25° to $\Delta\Theta_t$ = 0.125°, some $\approx$ 10% variation in C_P is observed with N_{OI} = 20, which is a small value compared to other trends. At λ = 2.36, the impact of azimuthal increment and outer iterations shows a different behavior. The C_P values are relatively higher and exhibit less variation with changes in $\Delta\Theta_t$. For N_{OI} = 10, N_{OI} = 20, and N_{OI} = 40, the C_P values remain around 0.22 to 0.28, irrespective of the azimuthal increment. Also, there exists no monotonously converging trend. At λ = 3.14, the C_P values show a similar trend to λ = 2.36 but with a slightly more noticeable variation. C_P prediction is dramatically high at $\Delta\Theta_t$ = 0.5° compared to finer temporal resolutions when N_{OI} is 20 or 40, while this variation is fairly small with N_{OI} = 10. This situation indicates that N_{OI} = 10 does not suffice for numerical convergence. C_P increases from $\Delta\Theta_t$ = 0.25° to 0.0625°, and N_{OI} = 20 and 40 results are almost identical, showing that performing more than N_{OI} = 20 iterations yield no improvement.

The simulation captures the aerodynamic performance more accurately with finer azimuthal increments and higher outer iterations, aligning more closely with the reference CFD and experimental values. As λ increases, the flow characteristics are less sensitive to the temporal resolution provided by the azimuthal increments, and a moderate number of outer iterations are sufficient to achieve convergence. The plots demonstrate that increasing N_{OI} from 10 to 40 generally enhances the predicted C_P, particularly at lower TSRs. However, beyond N_{OI} = 20, the improvement in C_P becomes marginal, suggesting a diminishing return on computational effort. Based on the analysis, an azimuthal increment of 0.125° and N_{OI} = 20 provide a good balance between accuracy and computational cost. At λ = 1.31, this combination yields a C_P close to the values obtained with finer increments and higher N_{OI} while significantly reducing the computational effort. Similarly, for λ = 2.36 and λ = 3.14, the chosen parameters produce C_P values that are in close agreement with the reference CFD and experimental results.

In conclusion, Mesh-B with D_{SMI} = 1.5D is used with an azimuthal increment of $\Delta\Theta_t$ = 0.125° and N_{OI} = 20 outer iterations in the rest of this study.

3.2 | Flow Around the Turbine Rotor

To provide a comprehensive understanding of the flow dynamics around a vertical axis wind turbine (VAWT), the vorticity contours along one rotation at different tip speed ratios are investigated in this section. By analyzing these contours, the individual power contribution of each turbine blade throughout a single rotation is explained. This analysis is necessary to identify the influence of varying tip speed ratios on the aerodynamic performance and efficiency of the VAWT. All flow fields presented are fully developed after at least 20 revolutions.

3.2.1 | SU2 Predictions Around the Near-rotor Region

The vorticity contours within the rotor and near-wake regions along a full rotation of the rotor are shown in Fig. 13 at three different TSRs. The Clockwise (CW) (negative) and Counter-Clockwise (CCW) (positive) rotating vortices can be seen as blue and red, respectively. The interval between each snapshot is $\Delta\Theta_R = 45^\circ$, and since each blade exhibits an almost identical power pattern, the flow state at every $\Theta_R = 15^\circ$ can be deduced from the figures.

The first notable observation is that the vortex patterns become more regularized as the λ increases. At $\lambda = 1.31$, the vortex shedding within the rotor region is much more complex and distinct compared to the other cases. Typically, positive and negative vortices are generated at the lower and upper surfaces of the blades, respectively. The Counter-Clockwise (CCW) rotating vortex generated at the lower surface of the blade detaches from the blade as it travels through the upstream portion of the rotor area (around $\Theta_R = 90 - 180^\circ$) due to the high negative angle of attack, which is then advected in the streamwise direction. This λ is particularly interesting because the linear speed of the blade closely matches the advection speed of the vortex trail at certain rotor azimuths, especially in the lower quarter arc of the swept circumference. The aforementioned strong vortex meets the blade from which it originated around $\Theta_R = 225 - 270^\circ$, resulting in a constant generation-and-collision of this vortex. Figure 14 shows the C_P contribution of Blade-1 with respect to Θ_R. When considered together with the contour plots, the effect of the aforementioned phenomenon is seen more clearly at $\lambda = 1.31$. The largest torque is generated around $\Theta_R = 45 - 90^\circ$. Some oscillatory behavior is evident between $\Theta_R = 90 - 120^\circ$, where the strong vortex detachment occurs. After this point and up to $\Theta_R = 0^\circ$, power generation remains close to zero.

At higher TSRs, a more structured helical trail is evident due to the wake constantly generated by each blade in a circular fashion, which is then advected in the $+x$ direction. As the blades rotate faster, the whole rotor starts acting like a semi-porous cylinder. Constant shedding of vortices occurs from the upper and lower parts of rotor area as shown in Fig. 13 with rotating in negative (blue) and positive (red) directions at $\Theta_R = 0^\circ$ and $\Theta_R = 180^\circ$, respectively. Similar observations were reported from wind tunnel experiments[37] and LES-type simulations.[38]

Different wake characteristics at $\lambda = 1.31$ than other simulated TSRs could be attributed to two factors. The dynamic solidity concept presented in[37] combines the geometrical solidity with turbine kinematics to quantify how much the turbine rotor effectively approaches the geometry of a circular cylinder in the flow. With λ, the dynamic solidity also increases, and the flow starts demonstrating vortex shedding and bluff-body characteristics. Another explanation lies in the thrust coefficient (C_T) of the rotor. As C_T becomes $C_T > 0.96$, the wake of a VAWT transitions from moment region to empirical state based on the momentum theory.[39] For this test case, C_T, as later shown in Fig. 18, jumps from $C_T \approx 0.7$ at $\lambda = 1.31$ to $C_T \approx 1$ at $\lambda = 2.36$ and stays at this level for $\lambda = 3.14$. This shows that the change of wake state from momentum region to empirical state coincides with the start of the observation of wake characteristics at $\lambda = 2.36$ similar to bluff-bodies.

The peak power production shifts towards the $\Theta_R = 60 - 150^\circ$ range, and the peak value increases with λ as seen in Fig. 14. However, negative torque regions also start to appear, becoming more noticeable with increasing λ. Specifically, at $\lambda = 3.14$, the rotation is high enough to keep each blade shadowed by the local wake of the blade in front of it, as there is not enough time for blade wakes to move out of the way by advection. In all cases, the blades pass through the vortex trail of the blade in front of them around $\Theta_R = 0 - 45^\circ$, which contributes to the negative power production seen in Fig. 14.

3.3 | Comparisons Between SU2 and OpenFOAM

This section compares the performance of SU2 and OpenFOAM in simulating the flow dynamics around the rotor and in the far-wake region of a Darrieus H-type VAWT. Vorticity contours are analyzed to understand the flow behavior in both the rotor area and the far wake. Additionally, power and thrust predictions from each solver are compared to each other and against experimental reference data. This examination is necessary to evaluate the accuracy and reliability of the solvers under different flow conditions and to understand how they handle complex aerodynamic phenomena. By assessing their performance, it is aimed to identify the strengths and weaknesses of each solver, which will inform future CFD studies and practical applications involving VAWTs. Identical grids and simulation parameters are used in both solvers, as presented in the previous sections.

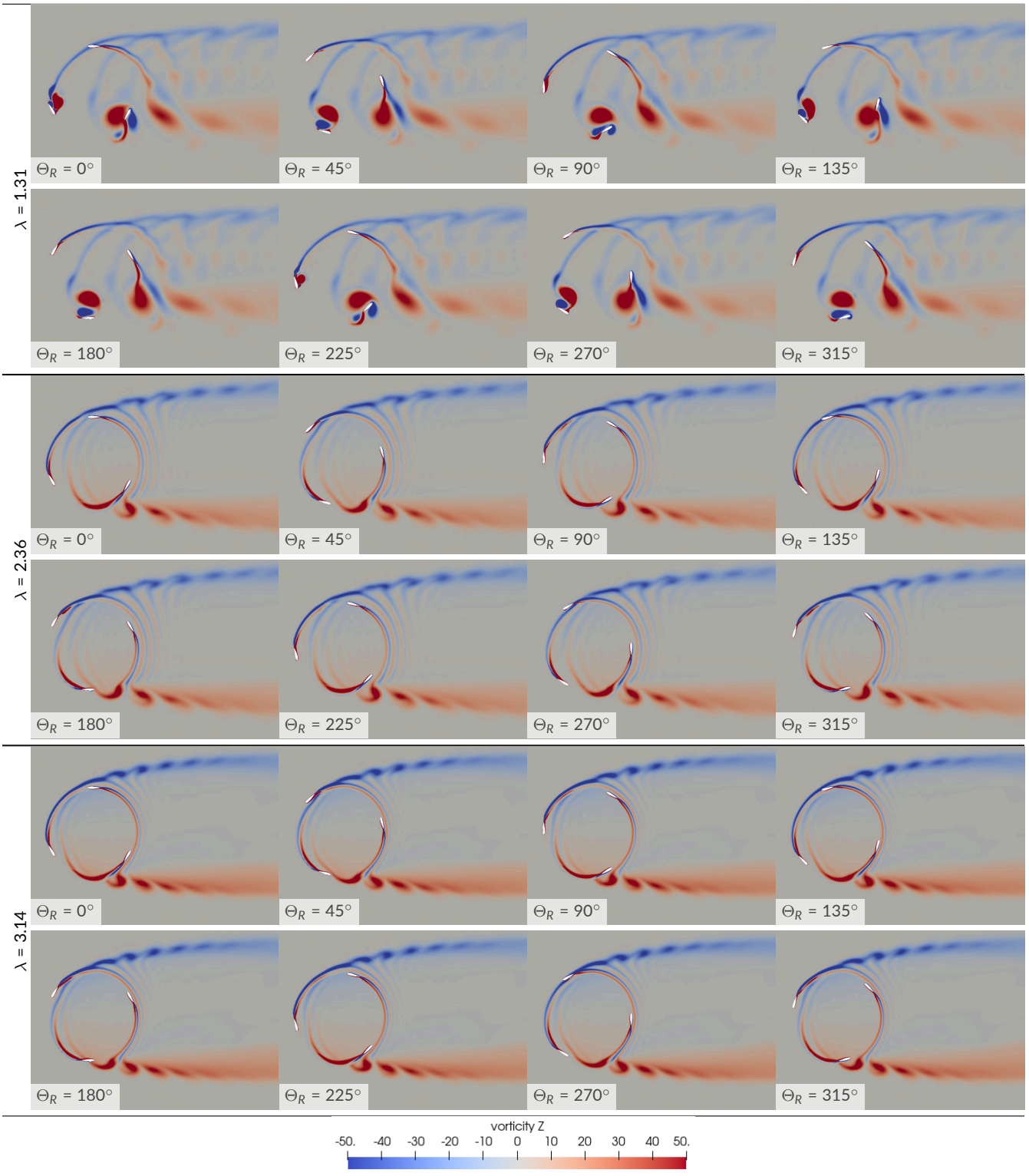

FIGURE 13 Vorticity (s^{-1}) contours around the rotor and near wake regions predicted by SU2 and shown for one revolution with 45° azimuthal steps at λ = 1.31 (top), λ = 2.36 (center), and λ = 3.14 (bottom)

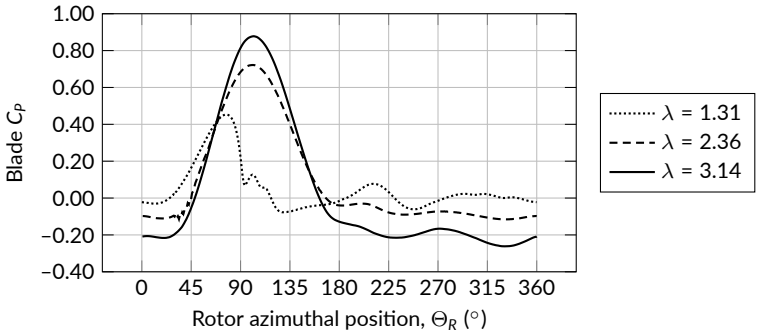

FIGURE 14 Power coefficient C_P variation of Blade-1 with rotor azimuthal position Θ_R at three different λ: 1.31, 2.36 and 3.14

3.3.1 | Wake Region

Figure 15 shows the vorticity contours around the rotor and near-wake regions at λ = 1.31, λ = 2.36, and λ = 3.14, as predicted by SU2 and OpenFOAM. The vorticity contours illustrate the rotational effects in the flow field, highlighting the differences in flow dynamics captured by the two solvers. In general, both solvers yield very close predictions qualitatively. At λ = 1.31, OpenFOAM shows well-defined vortical structures with clear shedding patterns near the rotor and in the wake region. The vortices appear more coherent and organized, suggesting a more stable prediction of the unsteady flow. In contrast, SU2 shows similar vortical structures but with slightly more diffuse and less organized patterns in the near-wake region. The negative vortex shed by the upstream blade is more pronounced, and its streamwise advection is clearly evident in OpenFOAM. At λ = 2.36, both solvers predict similar overall flow structures with distinct vortex shedding patterns. However, OpenFOAM's vorticity contours are more pronounced, with higher peak magnitudes of vorticity, indicating stronger rotational effects. SU2 also captures the main features but with less intensity in the vorticity peaks. At λ = 3.14, the flow becomes more complex with increased rotational speeds. OpenFOAM continues to show coherent and strong vortical structures, while SU2's vorticity contours are more diffused and spread out, although the difference is diminished. This discrepancy highlights the differences in how the two solvers handle higher TSRs and more complex flow dynamics. In summary, OpenFOAM generally predicts more coherent and intense vorticity structures compared to SU2. As the λ increases, the differences between the solvers become less pronounced, with SU2 maintaining clearer and stronger vortical patterns than lower λ predictions. These observations suggest that OpenFOAM might provide more accurate predictions of the unsteady flow dynamics, particularly in the rotor and near-wake regions. At the same time, SU2, although capturing the essential features, may require finer resolution or different numerical schemes to achieve similar levels of detail.

Figure 16 presents the vorticity contours in the far-wake region and the vortex shedding patterns from the rotor-swept area at three different TSRs, as predicted by SU2 and OpenFOAM. At λ = 1.31, both SU2 and OpenFOAM show the development of coherent vortex shedding from the rotor blades. The contours are similar up to 1D downstream. OpenFOAM captures the negative vortex shed by the upstream blade more clearly. Between 1D and 4D, distinct vortices shed from the top and bottom of the rotor area become visible. These vortices are outlined more clearly in OpenFOAM, while SU2 shows some diffusion. The wake structure differs dramatically between SU2 and OpenFOAM after 4D. The SU2 solution shows successive vortices rotating in opposite directions being stably advected all the way down to 13D downstream without mixing, whereas some formation of vortex street-like structures are visible in OpenFOAM. As λ increases, the solution in the rotor region becomes very similar between SU2 and OpenFOAM. Moreover, the von Kármán vortex street pattern becomes more evident, resembling those formed behind a cylinder in a crossflow. As λ gets higher, the location of shedding moves upstream, and the exact location also differs between the two solvers. At λ = 2.36, the shedding starts at around 5.5D in SU2 and 7D in OpenFOAM. Likewise, this location is predicted as 4D by SU2 and 5D by OpenFOAM at λ = 3.14. The distance between each subsequent counter-rotating shed vortices also varies at different TSRs, decreasing as the λ increases. In SU2, it is around 2.5D at λ = 2.36 and 2D at λ = 3.14. OpenFOAM predicts these distances as 3D at λ = 2.36 and 2.3D at λ = 3.14.

Overall, SU2 predicts an earlier initiation of shedding, while OpenFOAM yields a larger distance between the shed vortices. Another region that stands out is the near wake vortical structures that emanate from Θ_R = 240° of the rotor and extend up to 2D downstream in an arc shape, which is very clear in the OpenFOAM solution at λ = 2.36 and λ = 3.14 but diffused out in SU2.

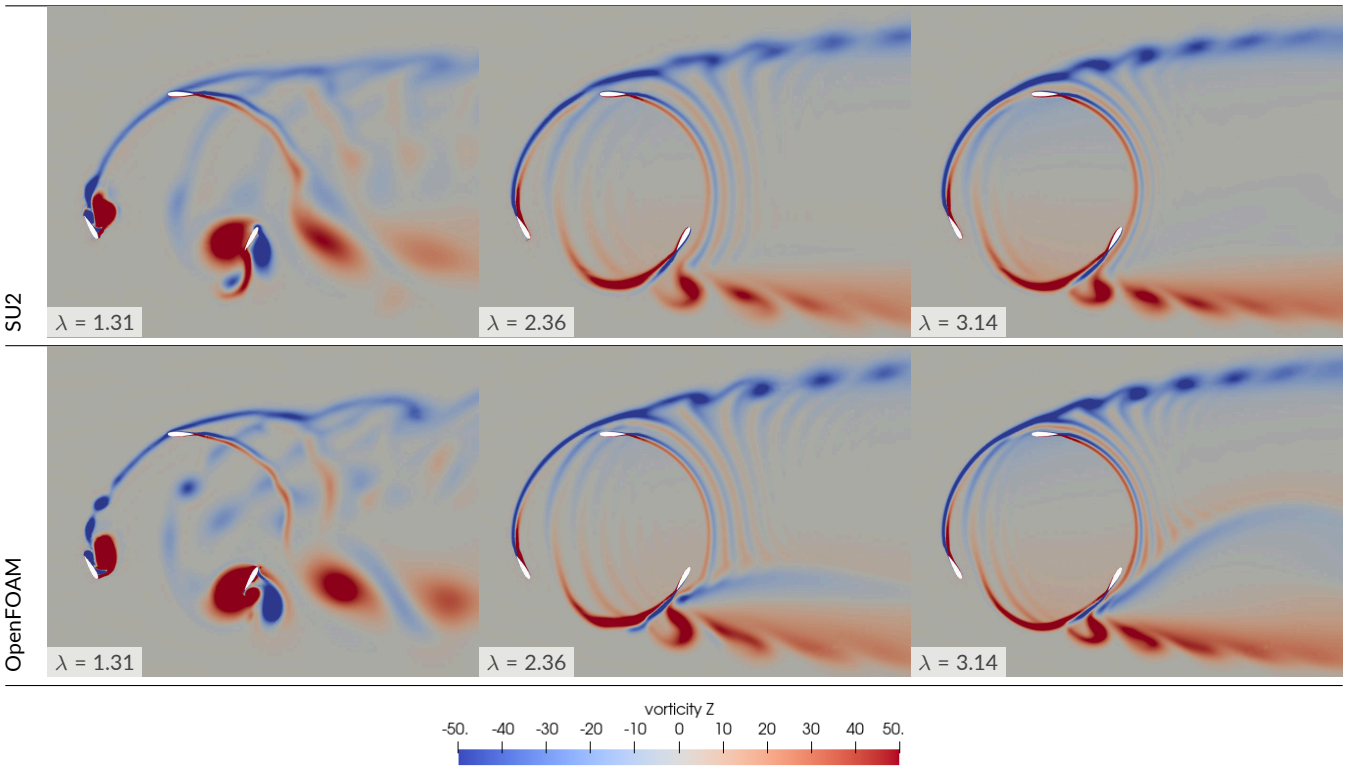

FIGURE 15 Vorticity (s^{-1}) contours around the rotor and near wake regions at various TSRs predicted by SU2 (top) and OpenFOAM (bottom) at λ = 1.31 (left), λ = 2.36 (center), and λ = 3.14 (right) with snapshots taken at Θ_R = 0°

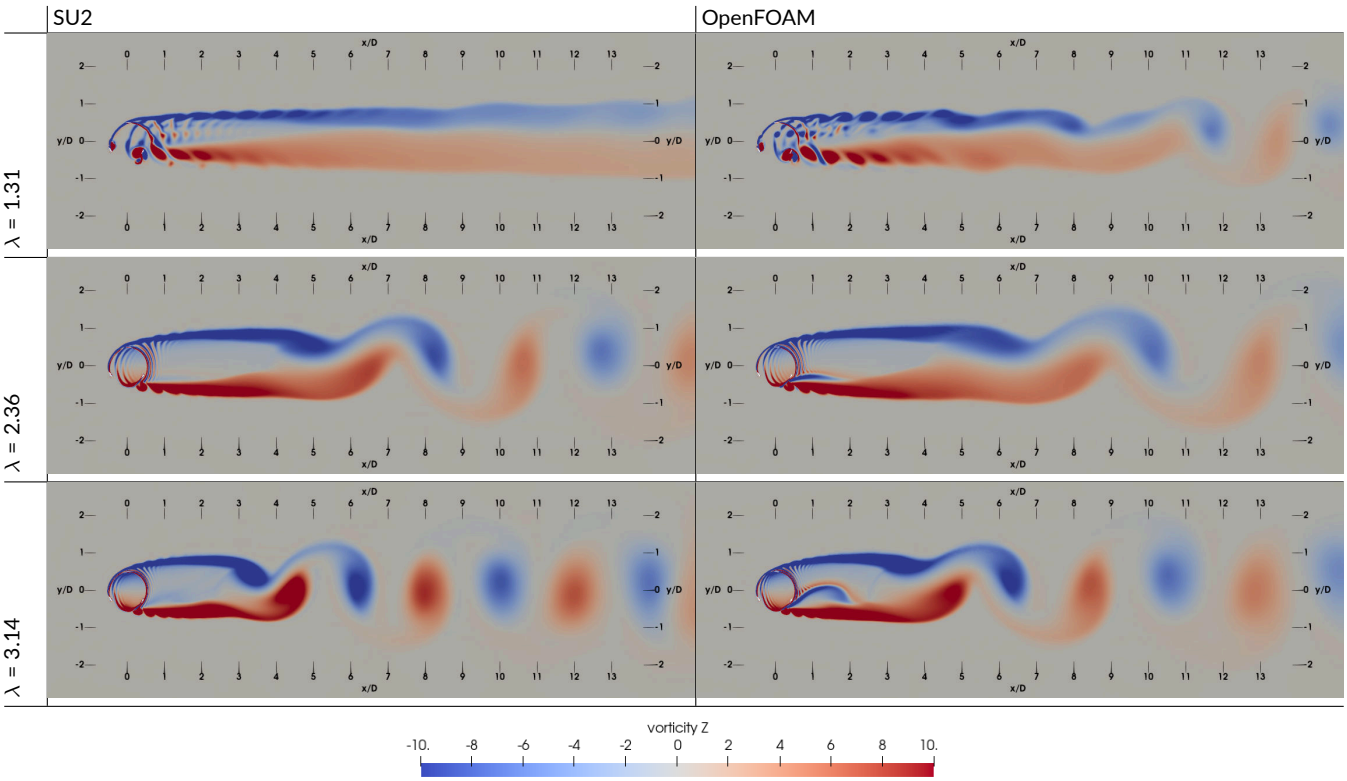

FIGURE 16 Vorticity (s^{-1}) contours in the far wake region and vortex shedding from the rotor swept area at various TSRs predicted by SU2 (left) and OpenFOAM (right) at λ = 1.31 (top), λ = 2.36 (middle), and λ = 3.14 (bottom) with snapshots taken at Θ_R = 0°

3.3.2 | Rotor Performance

Each blade of the VAWT experiences a wide range of angle of attack variations as the blade rotates around the rotational axis. Thus, the blade's lift and drag generation and the direction of the resultant force dramatically change. This affects the torque and, accordingly, power contribution to the turbine. In each simulation conducted for this study, the rotational speed and tip speed ratio are kept constant (i.e., the inertial effects are neglected). Hence, the torque directly corresponds to the power.

The variation of C_P contribution of a single blade and the total C_P of the rotor with respect to the rotor azimuthal position Θ_R are given in Fig. 17. SU2 and OpenFOAM predictions are mostly aligned at the medium and high TSRs, but some discrepancy exists at the lowest simulated λ. At λ = 1.31, the blade generates positive torque from Θ_R = 30° to 90°, i.e., only 1/6 of its total revolution. The blade imparts negative torque to the turbine between Θ_R = 90° and 180°. This is attributed to the freestream flow coming first towards the trailing edge, rather than towards the leading edge, of the retreating blade within this range and the blade being affected significantly because of its low rotational speed. The blade exhibits around zero torque in the downstream half of its revolution, where SU2 and OpenFOAM predictions agree very closely. However, SU2 predicts higher torque in the upstream half, although the power profiles are similar. The same case is seen in the rotor power profile, which is simply a summation of all three blades (bottom plots in Fig. 17). Due to this overprediction, C_P calculated by SU2 diverges from both the measurements and OpenFOAM predictions significantly but remains closer to the CFD study conducted by Balduzzi *et al.*[6], as shown in Fig. 18. Conversely, OpenFOAM's C_P prediction is close to the experimental data. Several previous studies have pointed to the *self-starting problem* that is inherent in VAWTs, making accurate power measurements difficult at low TSRs.[11] Thus, the uncertainty factor in the reference experimental data around λ = 1.31 should be noted.

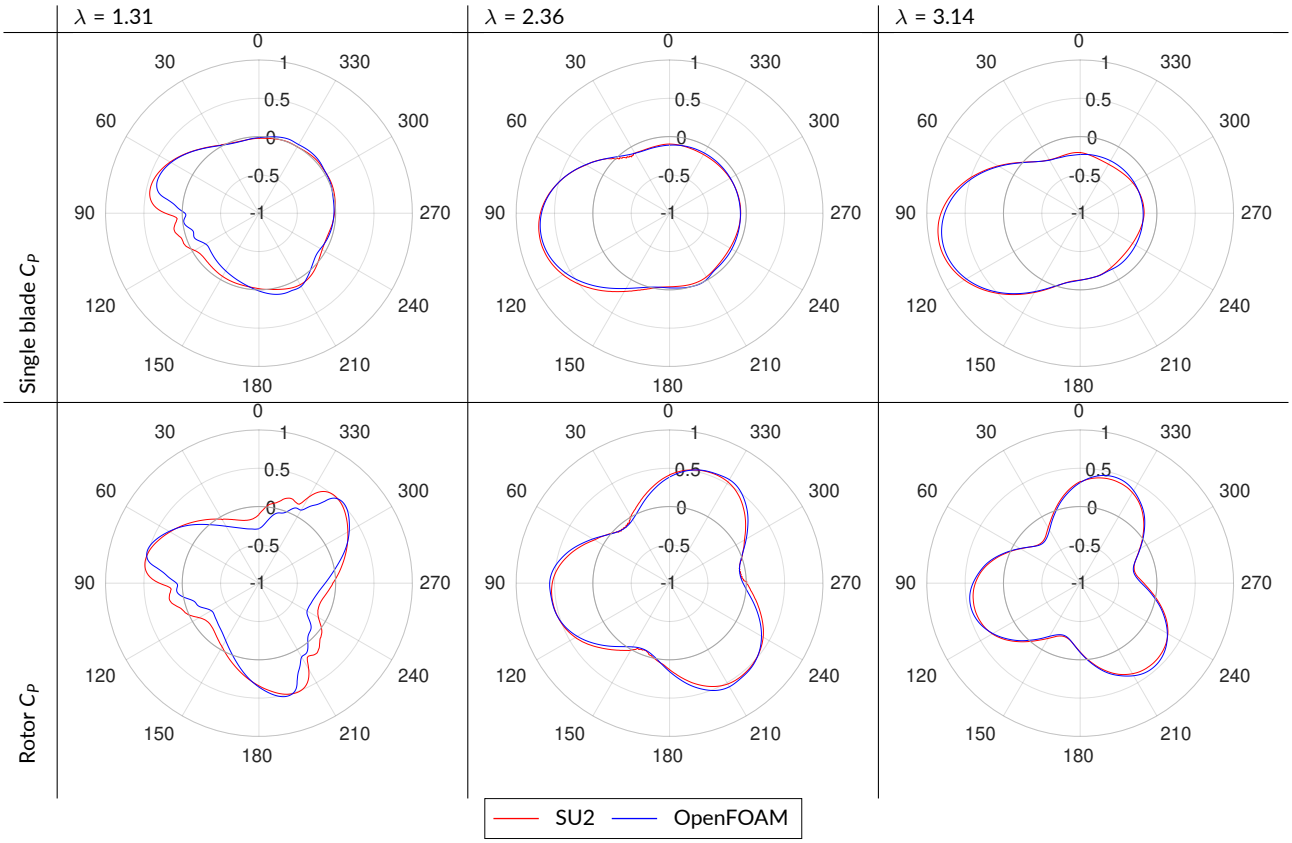

FIGURE 17 Variation of single blade (top) and rotor (bottom) power coefficient with rotor azimuthal position Θ_R (°) during the last three revolutions at λ = 1.31 (left), λ = 2.36 (center), and λ = 3.14 (right)

A further look to Fig. 17 reveals that the maximum torque generation of a single blade shifts towards the Θ_R = 45 – 160° range as λ gets higher. The negative torque region also shifts almost to the complete downstream half. At λ = 2.36, which is the rated λ of the VAWT where maximum C_P occurs, the negative power magnitude is minimal, as expected. The rotor power profile shows almost no negative power points. Interestingly,

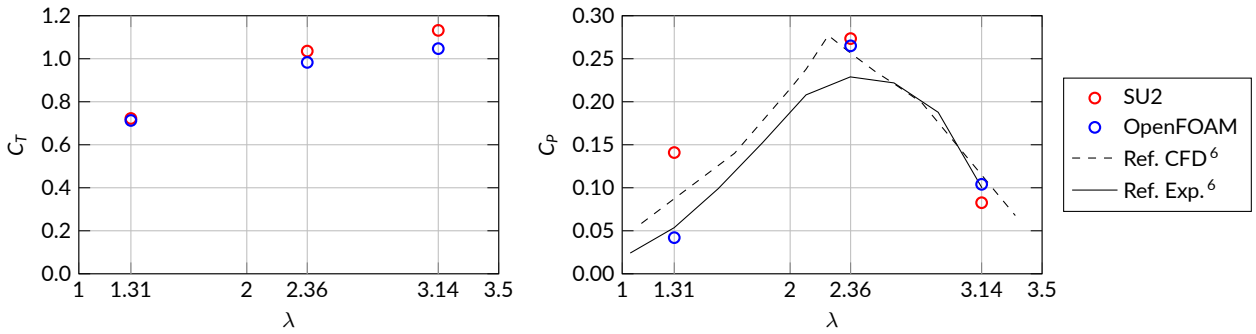

FIGURE 18 Predicted thrust coefficient C_T (left) and power coefficient C_P (right) at three different λ: 1.31, 2.36 and 3.14

the peak positive power is greater at $\lambda = 3.14$. However, each blade imparts a greater negative torque to the VAWT downstream (from $\Theta_R = 165°$ to $\Theta_R = 45°$) than at $\lambda = 2.36$, causing dramatic power loss during approximately 2/3 of its revolution compared to the rated λ. In both higher TSRs, the power profiles of SU2 and OpenFOAM align almost perfectly. The C_P difference between two solvers at the rated λ is only 6% and very close to the reference CFD. However, all CFD results diverge from the measurement by $\approx$ 15%. At $\lambda = 3.14$, all CFD results are closer to the experimental data, where OpenFOAM prediction overlaps with the reference data and the error of the SU2 prediction is 18%.

To further investigate why the SU2 and OpenFOAM power predictions are similar at high TSR but diverge at low TSR, the flow around Blade-1 is examined in greater detail in Fig. 19. In this figure, the pressure coefficient (c_p) field, which primarily governs the forces and moments, is plotted at $\lambda = 1.31$, along with the vorticity fields. Only the rotation through the upstream half of the rotor-swept area is considered ($\Theta_R < 180°$), where the largest discrepancies occur, as indicated by the single blade performance plot in Fig. 17. Here, the blade experiences a large negative relative incidence angle (α_{rel}). SU2 and OpenFOAM predict almost identical c_p and vorticity fields around the blade between $\Theta_R = 0-45°$ (where α_{rel} varies from 0° to approximately −20°, neglecting induction effects). This is also evident in the coinciding power profiles seen in Fig. 17. The first significant discrepancy appears around $\Theta_R = 75°$, which becomes visible in the c_p contours at $\Theta_R = 90°$. At this point, the single blade power predictions differ significantly between SU2 ($C_P \approx 0.25$) and OpenFOAM ($C_P \approx 0$). While the positive pressure fields at the upper surface are somewhat similar and the $c_p = 0$ points align closely, different suction fields are predicted at the lower surface. The relative incidence angle decreases from $\alpha_{rel} \approx -20°$ at $\Theta_R = 45°$ to its minimum value of $\alpha_{rel} \approx -50°$ at $\Theta_R = 135°$, and then increases back to $\alpha_{rel} \approx 0°$ at $\Theta_R = 180°$. The flow fields at $\Theta_R > 90°$ also reflect this trend. Although the vorticity fields at $\Theta_R = 135°$ appear similar, the pressure fields show a lack of agreement. While OpenFOAM predicts positive pressure at the lower surface up to 1/3 of the chord, SU2 results show complete suction. This pressure difference dies down at $\Theta_R = 165°$, where c_p is nearly zero around the airfoil in both SU2 and OpenFOAM, resulting in zero power, as shown in Fig. 17. Despite this, the vorticity fields still differ significantly, particularly in terms of the circulation of opposite signs in the leading edge vicinity and the CW-rotating shed vortex with distinct magnitudes near the lower surface.

Overall, while the pressure fields agree on the upper surface, the discrepancies in power predictions are mainly driven by differences on the lower surface. The trend suggests a strong correlation between the flow field disagreements and the relative incidence angle: as the angle of attack moves away from zero within the upstream half of the rotor, solvers diverge from each other. These discrepancies are attributed to numerical differences between SU2 and OpenFOAM, both of which employ distinct solution algorithms and flux schemes. Additionally, both codes utilize slightly different variants of turbulence models, which play a critical role, particularly in regions of strong flow separation and reattachment due to high angles of attack, as seen in the case above. There has been limited in-depth investigation into the root causes of discrepancies between the predictions of different CFD codes in the existing literature; however, similar findings have been reported in previous studies.[40,41,42]

Despite the discrepancies in C_P, the thrust coefficient predictions between SU2 and OpenFOAM are closer. For instance, at $\lambda = 1.31$, C_P predictions between SU2 and OpenFOAM diverge significantly, but C_T results are almost the same (Fig. 18). Conversely, C_T predictions slightly diverge as λ increases (8% at $\lambda = 3.14$), where C_P predictions are closer. A similar conclusion regarding thrust and power predictions was previously reported by Bangga et al.[43], where CFD simulations provided accurate thrust predictions for VAWTs but struggled to consistently predict power output. The thrust coefficient (C_T) depends on axial forces exerted on the rotor blades, influenced by blade geometry and overall flow field interaction. Since axial force results from pressure distribution over blade surfaces, it tends to be robust against minor differences in turbulence modeling and mesh resolution, keeping C_T predictions closer between the solvers at lower TSRs. Conversely, the power coefficient (C_P) relies on tangential forces and torque generated by the blades, which are sensitive to accurate angle of attack predictions and associated lift and drag forces. At lower TSRs, where flow conditions are more unsteady, slight differences in turbulence models, numerical schemes, and mesh resolution can significantly affect C_P predictions, causing divergence. Numerically, solver algorithms and turbulence models contribute to variations. SU2 and OpenFOAM handle

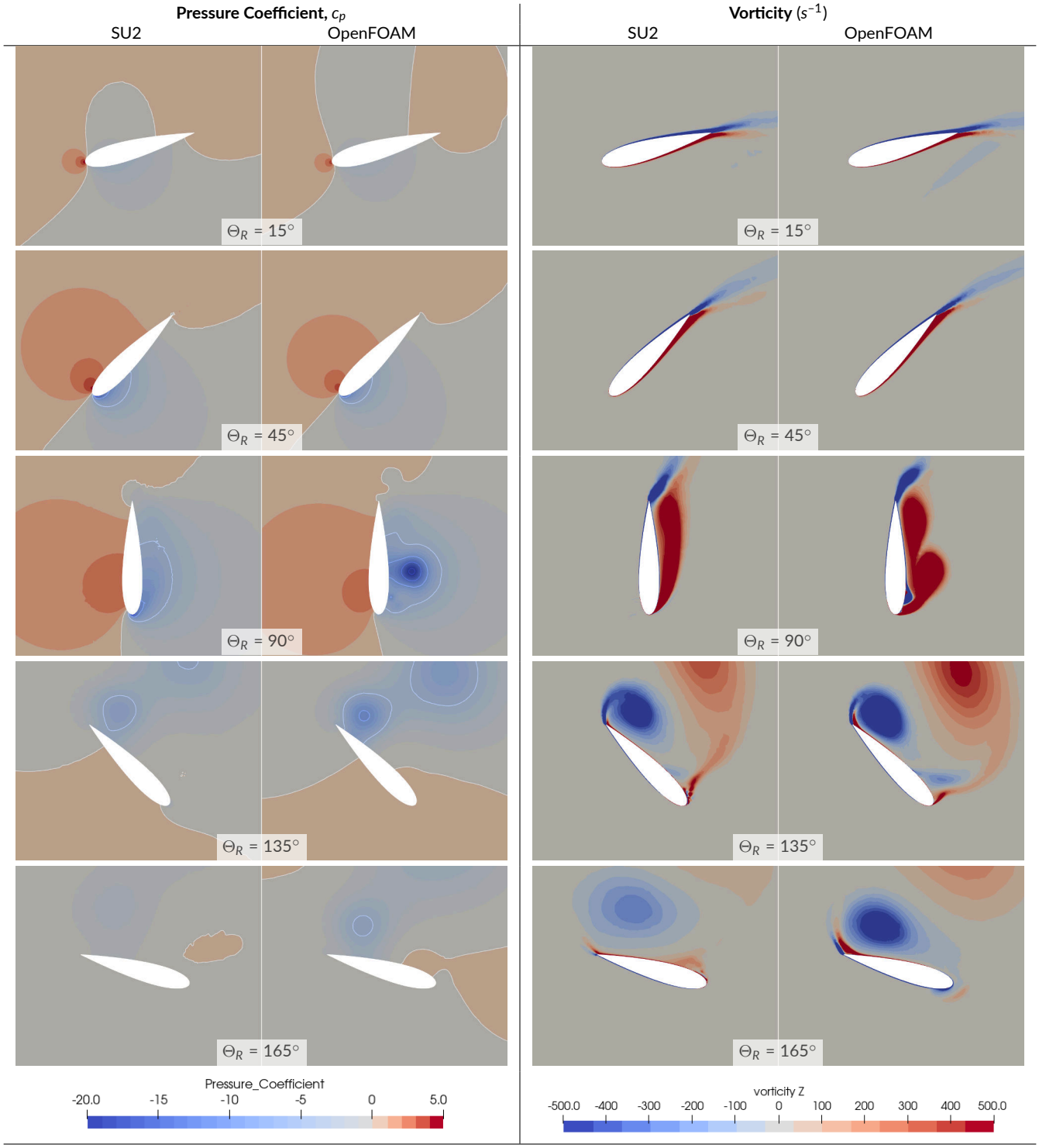

FIGURE 19 Pressure coefficient c_p and vorticity (s^{-1}) contours in the vicinity of a single blade as it travels along the upstream half of the rotor at λ = 1.31

discretization, turbulence modeling, and pressure-velocity coupling (incompressibility) differently. At lower TSRs, complex flow structures and unsteady effects make C_P prediction more sensitive to these numerical differences. The flow stabilizes as λ increases, reducing the C_P prediction sensitivity, hence resulting in a closer alignment. At higher TSRs, the C_T predictions diverge slightly due to the increasing influence of rotational effects on axial force. The flow is more affected by centrifugal and Coriolis forces, captured differently by the solvers, leading to slight C_T prediction variations.

3.4 | Parallel Computation Performance

The previously presented computations are performed on different systems equipped with Intel Xeon Platinum 8480+ and AMD Threadripper 3960x processors. To assess the computational performance and parallel scalability of SU2 and OpenFOAM, both solvers are executed with the simulation parameters detailed in the previous sections. The solution and algorithm controls are adjusted to be as identical as possible for both solvers to ensure a fair comparison. Linear solver tolerances are set to 10^{-7}, and the residual control is set to 10^{-5}. An azimuthal increment of $\Delta\Theta_t = 0.125^\circ$ is used, and the maximum number of outer (pseudo-time) iterations is limited to $N_{OI} = 20$.

The computational performance of the solvers from the first half-revolution of the rotor for $\lambda = 2.31$ are presented in Fig. 20. Their performances are assessed by the change of computational time, speedup, and computational efficiency with changing number of cores. Parallel speedup is defined as the ratio between the wall-clock time of the serial and parallel computations ($T_{serial}/T_{parallel}$), and the efficiency is the parallel speedup divided by the number of cores. It should be noted that as the flow develops, the required number of linear solver iterations decreases. Therefore, caution must be exercised when extrapolating wall-clock times to estimate performance over additional revolutions. Nonetheless, the relative performance indicators are expected to remain consistent.

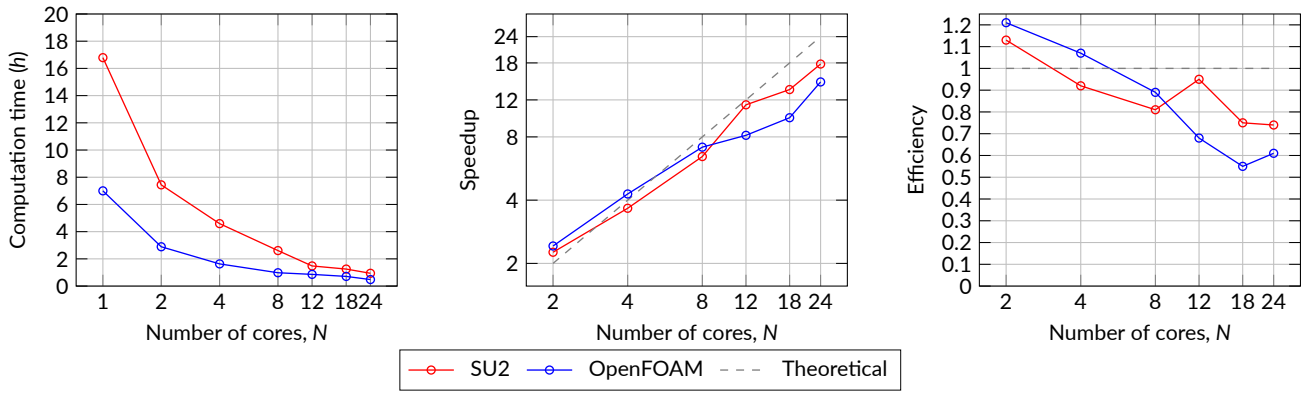

FIGURE 20 Parallel computational performance of SU2 and OpenFOAM simulations: computational wall clock time (left), computational speedup (center), and computational efficiency (right) changing with the number of cores

In terms of raw computational speed, OpenFOAM outperforms SU2 by a factor of 2.3 on average across all core counts. In a serial run, SU2 takes 2.6 times as long to complete as OpenFOAM. In parallel execution, OpenFOAM is 2.8 times faster than SU2 on 2 and 4 cores and approximately two times faster on larger core counts. This significant difference is attributed to the implementation of incompressibility in the solvers. OpenFOAM solvers are inherently incompressible and use algorithms specifically designed for pure incompressibility, while SU2 employs artificial incompressibility algorithms for infinite pressure propagation, which are known to offer lower computational performance.

Both solvers exhibit superlinear speedup on 2 cores, as shown in the efficiency graph. OpenFOAM and SU2 exceed the theoretical speedup limit by 20% and 10%, respectively. This is primarily due to the implementation of the algorithms and caching effects, a common occurrence in CFD codes due to the use of large cache memories as reported in previous studies.[44] OpenFOAM maintains superlinear speedup at 4 cores, whereas SU2 drops to 90% efficiency. The parallel performance of both solvers converges at 8 cores, after which SU2 outperforms OpenFOAM. On 12, 18, and 24 cores, SU2 provides better speedup and efficiency than OpenFOAM, although OpenFOAM still has a lower wall-clock time. The superior speedup and efficiency of SU2 with an increasing number of cores indicate that SU2 may offer better scalability for large-scale HPC applications, but further testing is needed to confirm this. The performance degradation is not monotonous for either solver, which may be caused by resource and cache contention, load imbalance, interference, and memory bandwidth limitations, as all simulations are executed simultaneously.

4 | CONCLUSIONS

Non-hierarchical domain decomposition methods are effectively employed to simulate unsteady and turbulent flow around a 2D rotating VAWT, incorporating dynamic grid motion and sliding mesh interfaces in parallel. The study is conducted at various tip speed ratios (TSRs). Since numerical and discretization parameters behave differently at different TSRs, sensitivity, and convergence studies are necessary for both low and high TSRs. Temporal convergence is particularly challenging at lower rotational speeds due to more complex flow dynamics. The grid resolution converged

with an equivalent SMI cell size of 0.012 m, which is 0.7% of the rotating region diameter or 4.9% of the blade chord. An azimuthal increment of $\Delta\Theta_t = 0.125^\circ$ per time step with 20 outer iterations is found to provide a stable solution and accurate power predictions. However, a finer spatial resolution could be required for the simulations at low TSRs where the rotor experiences significant blade-wake interactions, flow separation and vortical flow. The diameter of the rotating region has a negligible impact on power predictions, with 1.5 times the rotor diameter being sufficient. Similarly, while wake refinement does not significantly affect rotor performance predictions, it remains necessary to accurately capture wake dynamics. While larger azimuthal increments are sufficient for mid and high TSRs, accurate power prediction requires smaller increments. The vorticity contours in the rotor and near-wake regions at varying Tip Speed Ratios (TSRs) are investigated. As λ increases, vortex patterns become more regular, with complex shedding observed at the lowest TSR $\lambda = 1.31$. At higher TSRs, a structured helical wake forms, and the rotor exhibits characteristics similar to a porous cylinder with consistent Kármán vortex shedding. This transition could be attributed to the connection of rotor kinematics to the dynamic solidity concept or the transition of wake state to empirical region due to the increase in the thrust coefficient. The change in blade wake dynamics also affects the blade-wake interactions and, hence, the power production of the rotor. Power production peaks and shifts with increasing λ, but negative torque regions emerge due to the wake interactions between blades. The variations in C_P across different TSRs are investigated by comparing the predictions from SU2 and OpenFOAM simulations. At lower TSRs, the blade generates torque over only a small portion of its rotation, with discrepancies in the C_P predictions between the two solvers primarily due to the unsteady flow conditions and sensitivity to the numerical methods. As λ increases, the torque generation shifts, and the predictions from both solvers align more closely, though SU2 tends to overpredict the torque in the upstream half. The thrust predictions align more closely at lower TSRs due to robustness against the numerical differences, whereas power predictions may diverge due to sensitivity to the complex flow phenomena. At higher TSRs, stabilized flow reduces sensitivity in the C_P prediction, and rotational effects lead to slight divergences in the C_T predictions. In addition, the computational performance of two open-source CFD flow solvers, SU2 and OpenFOAM, are compared. SU2 underperforms in raw computational speed, which is attributed to its artificial methods for handling incompressible flows. In contrast, OpenFOAM exhibits poorer parallel speedup and efficiency, potentially due to its sequential solution algorithms compared to SU2's coupled methods; this warrants further investigation. Future investigations should focus on flow field interactions between $\lambda = 1.31$ and 2.36, where vortical structures vary significantly. Also, an in-depth examination of the numerical and algorithmic differences between OpenFOAM and SU2 is necessary to reveal the root causes of low-TSR discrepancies. Additionally, the parallel scalability of the two solvers with more cores should be explored.

AUTHOR CONTRIBUTIONS

Hüseyin Can Önel: Conceptualization (lead); formal analysis (lead); methodology (equal); software (equal); visualization; writing - original draft (lead). **Ali Ata Adam**: Conceptualization (supporting); formal analysis (supporting); methodology (equal); software (equal); writing - original draft (supporting); writing - review & editing. **Nilay Sezer Uzol**: Resources; supervision; writing - review & editing.

ACKNOWLEDGMENTS

The authors gratefully acknowledge the support of RÜZGEM (METUWIND) Center For Wind Energy Research and TÜBITAK ULAKBIM High Performance and Grid Computing Center for providing the computational resources for HPC and the Turkish National e-Science e-Infrastructure (TRUBA) supercomputers to run the parallel simulations.

FINANCIAL DISCLOSURE

None reported.

CONFLICT OF INTEREST

The authors declare no potential conflict of interest.

REFERENCES

1. Onel HC, Tuncer IH. Investigation of wind turbine wakes and wake recovery in a tandem configuration using actuator line model with LES. *Computers & Fluids*. 2021;220:104872. doi: 10.1016/j.compfluid.2021.104872
2. Adam AA, Deniz ON, Sezer-Uzol N, Uzol O. Determination of wake shapes behind a wind turbine through CFD simulations and comparison with analytical wake models. In: 11th Ankara International Aerospace Conference. 2021; Ankara.
3. Avila M, Gargallo-Peiró A, Folch A. A CFD framework for offshore and onshore wind farm simulation. *Journal of Physics: Conference Series*. 2017;854:012002. doi: 10.1088/1742-6596/854/1/012002
4. Nguyen VD, Jansson J, Goude A, Hoffman J. Direct Finite Element Simulation of the turbulent flow past a vertical axis wind turbine. *Renewable Energy*. 2019;135:238–247. doi: 10.1016/j.renene.2018.11.098
5. Steijl R, Barakos G. Sliding mesh algorithm for CFD analysis of helicopter rotor–fuselage aerodynamics. *International Journal for Numerical Methods in Fluids*. 2008;58(5):527–549. doi: 10.1002/fld.1757
6. Balduzzi F, Bianchini A, Maleci R, Ferrara G, Ferrari L. Critical issues in the CFD simulation of Darrieus wind turbines. *Renewable Energy*. 2016;85:419–435. doi: 10.1016/j.renene.2015.06.048
7. Balduzzi F, Bianchini A, Maleci R, Ferrara G, Ferrari L. Blade design criteria to compensate the flow curvature effects in H-Darrieus wind turbines. *Journal of Turbomachinery*. 2015;137(1):011006. doi: 10.1115/1.4028245

8. Maalouly M, Souaiby M, ElCheikh A, Issa J, Elkhoury M. Transient analysis of H-type Vertical Axis Wind Turbines using CFD. *Energy Reports*. 2022;8:4570–4588. doi: 10.1016/j.egyr.2022.03.136
9. Bianchini A, Balduzzi F, Bachant P, Ferrara G, Ferrari L. Effectiveness of two-dimensional CFD simulations for Darrieus VAWTs: a combined numerical and experimental assessment. *Energy Conversion and Management*. 2017;136:318–328. doi: 10.1016/j.enconman.2017.01.026
10. Meana-Fernández A, Fernández Oro JM, Argüelles Díaz KM, Galdo-Vega M, Velarde-Suárez S. Application of Richardson extrapolation method to the CFD simulation of vertical-axis wind turbines and analysis of the flow field. *Engineering Applications of Computational Fluid Mechanics*. 2019;13(1):359–376. doi: 10.1080/19942060.2019.1596160
11. Almohammadi K, Ingham D, Ma L, Pourkashan M. Computational fluid dynamics (CFD) mesh independency techniques for a straight blade vertical axis wind turbine. *Energy*. 2013;58:483–493. doi: 10.1016/j.energy.2013.06.012
12. Balduzzi F, Bianchini A, Ferrara G, Ferrari L. Dimensionless numbers for the assessment of mesh and timestep requirements in CFD simulations of Darrieus wind turbines. *Energy*. 2016;97:246–261. doi: 10.1016/j.energy.2015.12.111
13. Abdalrahman G, Melek W, Lien FS. Pitch angle control for a small-scale Darrieus vertical axis wind turbine with straight blades (H-Type VAWT). *Renewable Energy*. 2017;114:1353–1362. doi: 10.1016/j.renene.2017.07.068
14. Rossetti A, Pavesi G. Comparison of different numerical approaches to the study of the H-Darrieus turbines start-up. *Renewable Energy*. 2013;50:7–19. doi: 10.1016/j.renene.2012.06.025
15. Bianchini A, Balduzzi F, Ferrara G, Persico G, Dossena V, Ferrari L. A Critical Analysis on Low-Order Simulation Models for Darrieus Vawts: How Much Do They Pertain to the Real Flow?. *Journal of Engineering for Gas Turbines and Power*. 2018;141(1):011018. doi: 10.1115/1.4040851
16. Li Y, Yang S, Feng F, Tagawa K. A review on numerical simulation based on CFD technology of aerodynamic characteristics of straight-bladed vertical axis wind turbines. *Energy Reports*. 2023;9:4360–4379. doi: 10.1016/j.egyr.2023.03.082
17. Maître T, Amet E, Pellone C. Modeling of the flow in a Darrieus water turbine: Wall grid refinement analysis and comparison with experiments. *Renewable Energy*. 2013;51:497–512. doi: 10.1016/j.renene.2012.09.030
18. McNaughton J, Billard F, Revell A. Turbulence modelling of low Reynolds number flow effects around a vertical axis turbine at a range of tip-speed ratios. *Journal of Fluids and Structures*. 2014;47:124–138. doi: 10.1016/j.jfluidstructs.2013.12.014
19. Marten D, Bianchini A, Pechlivanoglou G, et al. Effects of Airfoil's Polar Data in the Stall Region on the Estimation of Darrieus Wind Turbine Performance. *Journal of Engineering for Gas Turbines and Power*. 2016;139(2):022606. doi: 10.1115/1.4034326
20. Weller HG, Tabor G, Jasak H, Fureby C. A tensorial approach to computational continuum mechanics using object-oriented techniques. *Computers in Physics*. 1998;12(6):620. doi: 10.1063/1.168744
21. Economon TD, Palacios F, Copeland SR, Lukaczyk TW, Alonso JJ. SU2: An Open-Source Suite for Multiphysics Simulation and Design. *AIAA Journal*. 2016;54(3):828–846. doi: 10.2514/1.J053813
22. Menter FR, Kuntz M, Langtry R. Ten Years of Industrial Experience with the SST Turbulence Model. In: Hanjalic K, Nagano Y, Tummers M., eds. *Turbulence, Heat and Mass Transfer 4*, Begell House, Inc., 2003:625-632.
23. Jain S, Saha UK. The State-of-the-Art Technology of H-Type Darrieus Wind Turbine Rotors. *Journal of Energy Resources Technology*. 2019;142(3):030801. doi: 10.1115/1.4044559
24. Menter FR. Two-equation eddy-viscosity turbulence models for engineering applications. *AIAA Journal*. 1994;32(8):1598–1605. doi: 10.2514/3.12149
25. Issa RI. Solution of the implicitly discretised fluid flow equations by operator-splitting. *Journal of Computational Physics*. 1986;62(1):40–65. doi: 10.1016/0021-9991(86)90099-9
26. Patankar S, Spalding D. A Calculation Procedure for Heat, Mass and Momentum Transfer in Three-Dimensional Parabolic Flows. *Numerical Prediction of Flow, Heat Transfer, Turbulence and Combustion*. 1983:54–73. doi: 10.1016/b978-0-08-030937-8.50013-1
27. Courant R, Friedrichs K, Lewy H. On the Partial Difference Equations of Mathematical Physics. *IBM Journal of Research and Development*. 1967;11(2):215–234. doi: 10.1147/rd.112.0215
28. Chevalier C, Pellegrini F. PT-Scotch: A tool for efficient parallel graph ordering. *Parallel Computing*. 2008;34(6–8):318–331. doi: 10.1016/j.parco.2007.12.001
29. Chorin AJ. A Numerical Method for Solving Incompressible Viscous Flow Problems. *Journal of Computational Physics*. 1997;135:118-125. doi: 10.1006/jcph.1997.5716
30. Economon TD. Simulation and Adjoint-Based Design for Variable Density Incompressible Flows with Heat Transfer. *AIAA Journal*. 2020;58(2):757–769. doi: 10.2514/1.J058222
31. Saad Y. A Flexible Inner-Outer Preconditioned GMRES Algorithm. *SIAM Journal on Scientific Computing*. 1993;14(2):461-469. doi: 10.1137/0914028
32. Windt C, Davidson J, Chandar DD, Faedo N, Ringwood JV. Evaluation of the overset grid method for control studies of wave energy converters in OpenFOAM numerical wave tanks. *Journal of Ocean Engineering and Marine Energy*. 2020;6(1):55–70. doi: 10.1007/s40722-019-00156-5
33. Dubas AJ, Bressloff NW, Sharkh SM. Numerical modelling of rotor-stator interaction in rim driven thrusters. *Ocean Engineering*. 2015;106:281–288. doi: 10.1016/j.oceaneng.2015.07.012
34. Economon T, Palacios F, Alonso J. Unsteady Aerodynamic Design on Unstructured Meshes with Sliding Interfaces. In: 51st AIAA Aerospace Sciences Meeting including the New Horizons Forum and Aerospace Exposition. 2013. doi: 10.2514/6.2013-632
35. Gomes P, Economon TD, Palacios R. Sustainable High-Performance Optimizations in SU2. In: AIAA Scitech 2021 Forum. 2021. doi: 10.2514/6.2021-0855
36. Rezaeiha A, Montazeri H, Blocken B. Towards accurate CFD simulations of vertical axis wind turbines at different tip speed ratios and solidities: Guidelines for azimuthal increment, domain size and convergence. *Energy Conversion and Management*. 2018;156:301–316. doi: 10.1016/j.enconman.2017.11.026
37. Araya DB, Colonius T, Dabiri JO. Transition to bluff-body dynamics in the wake of vertical-axis wind turbines. *Journal of Fluid Mechanics*. 2017;813:346–381. doi: 10.1017/jfm.2016.862
38. Abkar M, Dabiri JO. Self-similarity and flow characteristics of vertical-axis wind turbine wakes: an LES study. *Journal of Turbulence*. 2017;18(4):373–389. doi: 10.1080/14685248.2017.1284327

39. Ning A. Actuator cylinder theory for multiple vertical axis wind turbines. *Wind Energy Science*. 2016;1(2):327–340. doi: 10.5194/wes-1-327-2016
40. Strassburger CA, Liao W. Comparative Evaluation of Numerical Factors for their Effect on Prediction of Aerodynamic Forces and Moments in CFD. In: AIAA AVIATION 2022 Forum. 2022. doi: 10.2514/6.2022-3212
41. Murayama M, Lei Z, Mukai J, Yamamoto K. CFD validation for high-lift devices: Three-element airfoil. *Transactions of the Japan Society for Aeronautical and Space Sciences*. 2006;49(163):40–48. doi: 10.2322/tjsass.49.40
42. Klausmeyer SM, Lin JC. Comparative Results from a CFD Challenge Over a 2D Three-Element High-Lift Airfoil. Tech. Rep. NASA-TM-112858, National Aeronautics and Space Administration Langley Research Center; Hampton, Virginia: 1997.
43. Bangga G, Dessoky A, Wu Z, Rogowski K, Hansen MO. Accuracy and consistency of CFD and engineering models for simulating vertical axis wind turbine loads. *Energy*. 2020;206. doi: 10.1016/j.energy.2020.118087
44. Axtmann G, Rist U. Scalability of OpenFOAM with Large Eddy Simulations and DNS on High-Performance Systems. In: Nagel WE, Kröner DH, Resch MM., eds. *High Performance Computing in Science and Engineering ´16*, Cham: Springer International Publishing, 2016:413–424. doi: 10.1007/978-3-319-47066-5_28